

# First Stars XI. Chemical composition of the extremely metal-poor dwarfs in the binary CS 22876–032<sup>★</sup>

J. I. González Hernández<sup>1,2</sup>, P. Bonifacio<sup>1,2,3</sup>, H.-G. Ludwig<sup>1,2</sup>, E. Caffau<sup>2</sup>, M. Spite<sup>2</sup>, F. Spite<sup>2</sup>, R. Cayrel<sup>2</sup>, P. Molaro<sup>2,3</sup>, V. Hill<sup>2</sup>, P. François<sup>2</sup>, B. Plez<sup>5</sup>, T. C. Beers<sup>4</sup>, T. Sivarani<sup>4</sup>, J. Andersen<sup>6,7</sup>, B. Barbuy<sup>8</sup>, E. Depagne<sup>9</sup>, B. Nordström<sup>6</sup>, and F. Primas<sup>10</sup>

<sup>1</sup> CIFIST Marie Curie Excellence Team

<sup>2</sup> GEPI, Observatoire de Paris, CNRS, Université Paris Diderot; Place Jules Janssen 92190 Meudon, France  
e-mail: [Jonay.Gonzalez-Hernandez;Piercarlo.Bonifacio;Hans.Ludwig;Elisabetta.Caffau;Roger.Cayrel;  
;Monique.Spite;Francois.Spite;Vanessa.Hill;Patrick.Francois]@obspm.fr

<sup>3</sup> Istituto Nazionale di Astrofisica - Osservatorio Astronomico di Trieste, Via Tiepolo 11, I-34143 Trieste, Italy e-mail: molaro@ts.astro.it

<sup>4</sup> Department of Physics and Astronomy, CSCE: Center for the Study of Cosmic Evolution, and JINA: Joint Institute for Nuclear Astrophysics, Michigan State University, E. Lansing, MI 48824, USA  
e-mail: [thirupati;beers]@pa.msu.edu

<sup>5</sup> GRAAL, Université de Montpellier II, F-34095 Montpellier Cedex 05, France  
e-mail: Bertrand.Plez@graal.univ-montp2.fr

<sup>6</sup> The Niels Bohr Institute, Astronomy, Juliane Maries Vej 30, DK-2100 Copenhagen, Denmark  
e-mail: [ja;birgitta]@astro.ku.dk

<sup>7</sup> Nordic Optical Telescope, Apartado 474, E-38700 Santa Cruz de La Palma, Spain  
e-mail: ja@not.iac.es

<sup>8</sup> Universidade de Sao Paulo, Departamento de Astronomia, Rua do Matao 1226, 05508-900 Sao Paulo, Brazil  
e-mail: barbuy@astro.iag.usp.br

<sup>9</sup> Las Cumbres Observatory, Goleta, CA 93117, USA  
e-mail: edepagne@lcogt.net

<sup>10</sup> European Southern Observatory (ESO), Karl-Schwarzschild-Str. 2, D-85749 Garching b. München, Germany  
e-mail: fprimas@eso.org

Received July, 2007; accepted –

## ABSTRACT

**Context.** Unevolved metal-poor stars constitute a fossil record of the Early Galaxy, and can provide invaluable information on the properties of the first generations of stars. Binary systems also provide direct information on the stellar masses of their member stars. **Aims.** The purpose of this investigation is a detailed abundance study of the double-lined spectroscopic binary CS 22876–032, which comprises the two most metal-poor dwarfs known.

**Methods.** We have used high-resolution, high-S/N ratio spectra from the UVES spectrograph at the ESO VLT telescope. Long-term radial-velocity measurements and broad-band photometry allow us to determine improved orbital elements and stellar parameters for both components. We use OSMARCS 1D models and the TURBOSPECTRUM spectral synthesis code to determine the abundances of Li, O, Na, Mg, Al, Si, Ca, Sc, Ti, Cr, Mn, Fe, Co and Ni. We also use the CO<sup>5</sup>BOLD model atmosphere code to compute the 3D abundance corrections, especially for Li and O.

**Results.** We find a metallicity of  $[\text{Fe}/\text{H}] \sim -3.6$  for both stars, using 1D models with 3D corrections of  $\sim -0.1$  dex from averaged 3D models. We determine the oxygen abundance from the near-UV OH bands; the 3D corrections are large,  $-1$  and  $-1.5$  dex for the secondary and primary respectively, and yield  $[\text{O}/\text{Fe}] \sim 0.8$ , close to the high-quality results obtained from the [OI] 630 nm line in metal-poor giants. Other  $[\alpha/\text{Fe}]$  ratios are consistent with those measured in other dwarfs and giants with similar  $[\text{Fe}/\text{H}]$ , although Ca and Si are somewhat low ( $[\text{X}/\text{Fe}] \lesssim 0$ ). Other element ratios follow those of other halo stars. The Li abundance of the primary star is consistent with the Spite plateau, but the secondary shows a lower abundance; 3D corrections are small.

**Conclusions.** The Li abundance in the primary star supports the extension of the *Spite Plateau* value at the lowest metallicities, without any decrease. The low abundance in the secondary star could be explained by endogenic Li depletion, due to its cooler temperature. If this is not the case, another, yet unknown mechanism may be causing increased scatter in  $A(\text{Li})$  at the lowest metallicities.

**Key words.** nuclear reactions, nucleosynthesis, abundances – Galaxy:halo – Galaxy:abundances – cosmology:observations – stars: Population II

Send offprint requests to: J. I. González Hernández

<sup>★</sup> Based on observations made with the ESO Very Large Telescope at Paranal Observatory, Chile (Large Programme “First Stars”, ID 165.N-0276(A); P.I. R. Cayrel).

## 1. Introduction

Extremely metal-poor (EMP) stars formed with the chemical composition of the gas in the early Galaxy, and constitute a unique source of information on the first generations of stars. Among EMP stars, a special place is held by the dwarfs, which

are not subject to the mixing episodes experienced by giants, thus enhancing their value as cosmological probes.

In fact, among these stars the Li abundance appears to be constant whatever the stellar temperature or metallicity (Spite & Spite 1982a,b), the *Spite plateau*. The simplest interpretation of the plateau is that it represents the primordial Li abundance, i.e., it reflects the amount of Li formed in the first minutes of the existence of the Universe. If so, Li can be used as a “baryometer”, a tool to measure the baryonic density of the Universe, since this is the only cosmological parameter upon which the primordial Li abundance depends upon.

The independent determination of the baryonic density from the fluctuations of the Cosmic Microwave Background by the WMAP satellite (Spergel et al. 2003, 2007) and other CMB experiments measuring fluctuations on smaller angular scales, such as the VSA (Rebolo et al. 2004; Grainge et al. 2003), ACBAR (Kuo et al. 2004) and CBI (Pearson et al. 2003) experiments, implies a primordial Li abundance which is at least a factor of 3–4 larger than that observed on the *Spite plateau*, creating a conflict with the traditional interpretation of the plateau.

In Paper VII in this series (Bonifacio et al. 2007) we have investigated the *Spite plateau* at the lowest metallicities (down to  $[\text{Fe}/\text{H}] = -3.3$ ) and found marginal evidence that at these low metallicities there could be an increased scatter or even a sharp drop in the Li abundance. It is therefore of great interest to explore the Li abundance in stars of even lower metallicity.

The star CS 22876–032 was identified in the first paper reporting results of the HK objective-prism survey by Beers et al. (1985), who noted that it had the weakest Ca II K line in the low-metallicity sample, suggesting that it could be as metal-deficient as the record holder at that time, the giant CD -38°245 (Bessell & Norris 1984). CS 22876–032 had already been observed in the objective-prism survey of Slettebak & Brundage (1971), who classified it as an A-type peculiar star and noted its weak and diffuse Balmer lines. Having assigned to this star a much earlier spectral type, they did not conclude that the weakness of the Ca II K line was indeed due to an extremely low metallicity.

At the conference “Chemical and Dynamical Evolution of Galaxies” in 1989 (Bonifacio et al. 1990), P. Molaro announced that high-resolution spectra from the CASPEC spectrograph at the ESO 3.6 m telescope indicated  $[\text{Fe}/\text{H}] \sim -4.3$  for CS 22876–032. However, just afterwards Nissen (1989) discovered, from similar-resolution spectra, that the star is a double-lined spectroscopic binary. The spectra acquired by Molaro were obtained at a single-lined phase, and the abundance analysis of CS 22876–032 by Molaro & Castelli (1990) assumed that it was a single star. Thus, veiling was neglected, the adopted temperature was too low, and the measured  $[\text{Fe}/\text{H}]$  was therefore a lower limit to the metallicity of the system.

Although CS 22876–032 is relatively bright ( $V=12.84$ ) for an EMP star, it took another ten years before a sufficient number of high-resolution spectra had been accumulated to allow to determine of the orbital parameters of this system, and to perform a consistent chemical analysis. Norris, Beers, & Ryan (2000) found the orbital period to be 424.7 days and the metallicity of the system  $[\text{Fe}/\text{H}] = -3.71$ . In spite of the upward revision of the metallicity, partly due to the different solar Fe abundance assumed ( $\log \epsilon(\text{X})_{\odot} = 7.50$  instead of 7.63 in Molaro & Castelli 1990), the two stars in CS 22876–032 remain the most metal-poor dwarfs known.

Thus, the CS 22876–032 system constitutes a unique fossil, recording the chemical composition of the early Galaxy. Moreover, it allows a measurement of the Li abundance which

probes the *Spite plateau* at a lower metallicity than any other known dwarfs. Note that, despite its the extremely low iron abundance ( $[\text{Fe}/\text{H}] = -5.4$ ), the star HE 1327–2326 (Frebel et al. 2005) has very high C, N and O abundances, so its global metallicity,  $Z$ , is considerably higher than that of CS 22876–032. It has also been shown recently that this star is most likely a slightly evolved subgiant, not a dwarf.

In this paper we use high-resolution, high-S/N ratio spectra from the ESO Kueyen 8.2m telescope and the UVES spectrograph to improve the orbital solution and perform a complete chemical analysis of the two stars that comprise CS 22876–032. With respect to the Norris, Beers, & Ryan (2000) analysis, our superior S/N ratio and larger spectral coverage permit measurement of abundances for many more elements, and, most importantly, for *both* components; the Norris, Beers, & Ryan (2000) analysis of the secondary star was limited to Fe.

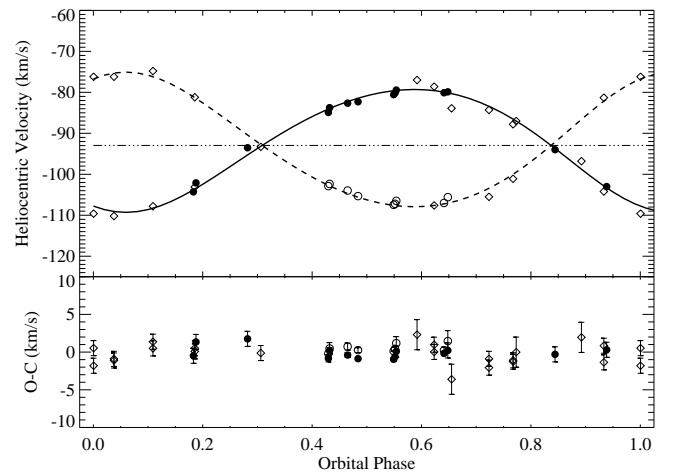


**Fig. 1.** Upper panel: Radial velocities of CS 22876–032 (filled circles: A; open circles: B). Open diamonds: Data from Norris et al. (2000). The curves show the orbital solution ( $P = 425$  d,  $e = 0.14$ ) for Star A (solid) and B (dashed). Dot-dashed horizontal line: Centre-of-mass velocity of the system. Lower panel: Residuals from the fit.

## 2. Observations and data reduction

Spectroscopic observations of the CS 22876–032 were carried out with the UV-Visual Echelle Spectrograph (UVES, Dekker et al. 2000) at the European Southern Observatory (ESO), *Observatorio Cerro Paranal*, using the 8.2 m VLT-Kuyen telescope on 2000 July 19, 20, August 3, 11, and October 17, 20, and 2001 November 7, 8 and 9, covering the spectral region from 300.0 nm to 1040.0 nm. Most of the observations were made with a projected slit width of  $1''$  at a resolving power  $\lambda/\delta\lambda \sim 43\,000$ . The spectra were reduced in a standard manner using the UVES reduction package within the MIDAS environment. The signal-to-noise ratio per pixel varies from 25 at 312.0 nm, 50 at 330.0 nm up to 150 or higher above 410.0 nm.

**Table 1.** Radial-velocity observations of CS 22876–032. For each velocity,  $\sigma$  is the estimated error and  $(O-C)$  the residual from the orbital fit. \*:  $H_\alpha$  velocities; omitted from solution.

Date (days)	HJD-2,400,000	Phase km s <sup>-1</sup>	$V_A$ km s <sup>-1</sup>	$\sigma V_A$ km s <sup>-1</sup>	$(O-C)_A$ km s <sup>-1</sup>	$V_B$ km s <sup>-1</sup>	$\sigma V_B$ km s <sup>-1</sup>	$(O-C)_B$	Source
1985 Sep 6 .....	46315.1	0.669	-83.9	2.0	-3.44	–	–	–	NBR00
1985 Dec 16 .....	46416.0	0.907	-96.8	2.0	1.72	–	–	–	NBR00
1988 Sep 27 .....	47431.7	0.297	-93.5	1.0	1.44	–	–	–	MC90
1989 Sep 13 .....	47783.2	0.124	-107.8	1.0	0.63	-74.8	1.0	1.48	NBR00
1989 Oct 15 .....	47814.6	0.199	-104.3	1.0	-0.94	–	–	–	NBR00
1989 Oct 16 .....	47815.7	0.201	-103.1	1.0	0.07	-81.2	1.0	0.86	NBR00
1989 Oct 17 .....	47816.6	0.204	-102.1	1.0	0.87	–	–	–	NBR00
1989 Dec 6 .....	47867.0	0.322	-93.3	1.0	-0.35	–	–	–	NBR00
1990 Sep 1 .....	48135.7	0.955	-103.0	1.0	0.83	–	–	–	CASPEC
1990 Sep 27 .....	48162.1	0.017	-109.6	1.0	-0.91	-76.2	1.0	-0.20	NBR00
1991 May 23 .....	48400.0*	0.577	-87.5	2.0	-7.34	–	–	–	EMMI
1991 Aug 22 .....	48490.5	0.790	-87.0	2.0	-0.47	–	–	–	NBR00
1991 Sep 21 .....	48520.7	0.861	-94.0	1.0	-0.65	–	–	–	EMMI
1992 Aug 17 .....	48851.8	0.640	-78.6	1.0	1.41	-107.6	1.0	-0.12	NBR00
1992 Dec 12 .....	48967.5*	0.912	-90.9	2.0	8.33	–	–	–	EMMI
1996 Aug 7 .....	50303.1	0.057	-110.2	1.0	-0.28	-76.2	1.0	-1.55	NBR00
1997 Aug 23 .....	50683.8	0.957	-104.2	1.0	-0.57	-81.3	1.0	0.25	NBR00
1998 Aug 12 .....	51038.3	0.787	-87.8	1.0	-1.47	-101.1	1.0	-0.56	NBR00
1999 Jul 29 .....	51388.7	0.612	-77.0	2.0	2.89	–	–	–	NBR00
1999 Sep 23 .....	51444.6	0.744	-84.3	1.0	-0.93	-105.5	1.0	-1.71	NBR00
2000 Jul 19 .....	51744.8	0.451	-84.9	0.5	-0.52	-102.9	0.3	-0.22	VLT
2000 Jul 20 .....	51745.8	0.453	-83.7	0.4	0.56	-102.3	0.8	0.51	VLT
2000 Aug 3 .....	51759.8	0.486	-82.6	0.3	0.13	-103.9	0.5	0.59	VLT
2000 Aug 11 .....	51767.9	0.505	-82.3	0.3	-0.31	-105.3	0.3	0.01	VLT
2000 Oct 17 .....	51834.7	0.662	-80.1	0.3	0.22	-107.0	0.4	0.14	VLT
2000 Oct 20 .....	51837.6	0.669	-79.9	1.0	0.56	-105.6	1.4	1.38	VLT
2001 Nov 7 .....	52220.6	0.571	-80.6	0.3	-0.35	-107.4	0.3	-0.18	VLT
2001 Nov 8 .....	52221.6	0.573	-80.2	0.3	0.01	-107.2	0.3	0.06	VLT
2001 Nov 9 .....	52222.6	0.575	-79.4	0.7	0.78	-106.6	0.9	0.69	VLT

Sources: NBR00: Norris, Beers, & Ryan (2000, and references therein); MC90: Molaro & Castelli (1990); CASPEC: Unpublished velocity from a Caspec spectrum; EMMI: Unpublished velocities from EMMI spectra; VLT: This paper.

**Table 2.** Orbital elements of CS 22876–032

Parameter	This paper	Norris et al. (2000)
$P$ (days)	$424.81 \pm 0.37$	$424.71 \pm 0.60$
$T_0$ (HJD–2,400,000)	$48579.8 \pm 7.1$	$48576.4 \pm 13.5$
$e$	$0.143 \pm 0.013$	$0.12 \pm 0.03$
$w$ (deg)	$148.1 \pm 6.4$	$144.96 \pm 12.4$
$V_0$ (km s <sup>-1</sup> )	$-93.11 \pm 0.13$	$-93.36 \pm 0.28$
$K_A$ (km s <sup>-1</sup> )	$15.04 \pm 0.26$	$15.13 \pm 0.51$
$K_B$ (km s <sup>-1</sup> )	$16.51 \pm 0.27$	$17.06 \pm 0.56$
$M_A \sin^3 i (M_\odot)$	$0.701 \pm 0.021$	$0.76 \pm 0.04$
$M_B \sin^3 i (M_\odot)$	$0.639 \pm 0.019$	$0.68 \pm 0.04$
$M_B/M_A$	$0.911 \pm 0.022$	$0.89 \pm 0.04$
$\sigma$ (km s <sup>-1</sup> )	1.01	1.60

### 3. Revised orbital parameters

We derived radial velocities from the UVES spectra by fitting a Gaussian to several unblended spectral lines within the IRAF<sup>1</sup> context. Table 1 contains the radial velocities and the 1- $\sigma$  er-

rors estimated from the dispersion of the measurements of different stellar lines. We also list other velocity data given by Norris, Beers, & Ryan (2000) and references therein, or which we have measured from previously unpublished CASPEC or EMMI spectra of this system.

Here and in the rest of the paper, we denote the more massive and luminous primary star as Star A, the secondary as Star B.

Our new radial-velocity measurements of CS 22876–032 extend the time coverage of its orbit considerably and permit improvement of the orbital elements relative to those by published by Norris, Beers, & Ryan (2000). The computed orbital parameters are given in Table 2; Fig. 1 compares the observed radial velocities of both stars with the curves predicted from these orbital elements.

Note especially the improved mass ratio,  $M_B/M_A = 0.91 \pm 0.02$ , which provides stringent constraints on the stellar parameters for the two components of the binary as discussed below. Note also that the orbital eccentricity is the lowest found among halo spectroscopic binaries with periods in the range 100–2000 days (see Latham et al. 2002; Goldberg et al. 2002). While this might be a hint that tidal interaction has been strong in this system, perhaps in the pre-main-sequence phase, the separation of the stars has been so large throughout their main-sequence life that this is unlikely to be the cause of the apparent Li depletion we find in star B (see Sect. 6.1).

<sup>1</sup> IRAF is distributed by National Optical Astronomy Observatory, which is operated by the Association of Universities for Research in Astronomy, Inc., under contract with the National Science Foundation.

## 4. Model Atmospheres

### 4.1. One-dimensional models

Our analysis used OSMARCS 1D LTE model atmospheres (Gustafsson et al. 1975; Plez et al. 1992; Edvardsson et al. 1993; Asplund et al. 1997; Gustafsson et al. 2003) and the TURBOSPECTRUM spectral synthesis code (Alvarez & Plez 1998). Models were interpolated in pre-computed grids for a metallicity of  $[\text{Fe}/\text{H}] = -3.6$ , since this was the final iron abundance (see § 5.2), and with an  $\alpha$ -element enhancement of  $[\alpha/\text{Fe}] = +0.4$  dex. We adopted solar abundances from Grevesse & Sauval (2000), with the exception of O, for which we adopted  $\log \epsilon(\text{O})_{\odot} = 8.72$ , based on 3D model atmospheres (Ludwig & Steffen 2007; Caffau et al. 2007b). The code TURBOSPECTRUM is used to determine 1D element abundances in each component of the binary, either via spectrum synthesis or by comparing the observed equivalent widths of different stellar lines with the theoretical curves of growth (see § 5.2).

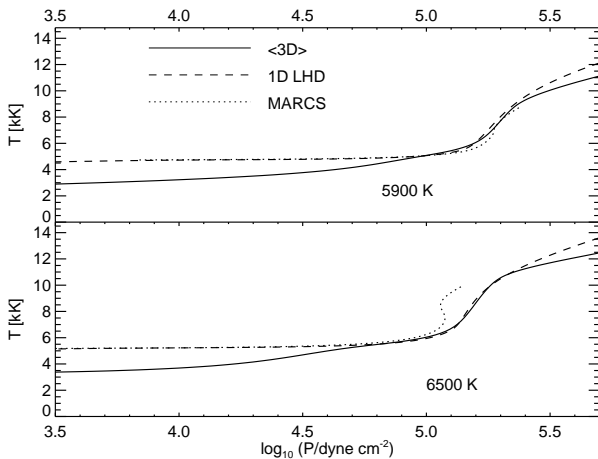


**Fig. 2.** Average temperature profile of 3D CO<sup>5</sup>BOLD atmospheric models (solid lines) compared to 1D<sub>LHD</sub> (dashed) and 1D MARCS models (dotted) in stars A (bottom panel) and B (top).

### 4.2. Three-dimensional models

In this work we also consider two 3D model atmospheres, which have been computed with the CO<sup>5</sup>BOLD code (Freytag et al. 2002; Wedemeyer et al. 2003), one for each star. The atmospheric parameters are close to those observed for the two stars:  $T_{\text{eff}}/\log g/[\text{Fe}/\text{H}]$ : 6550/4.50/−3.0 (A) and 5920/4.50/−3.0 (B). Each model consists of a representative set of snapshots sampling the temporal evolution of the photospheric flow at equal intervals in time. The total time intervals were 2400 s for the warmer star A, and 9500 s for the cooler star B. These time intervals should be compared to the convective turn-over timescales. From the hydrodynamical point of view, typical timescales in the models for both components are not much different from that in a solar model, where the convective turn-over timescale amounts to about 500 s. Thus, we sample about five turn-over timescales for the hotter and almost twenty for the cooler component.

The comparison of 3D vs. 1D models depends on which particular 1D model is chosen. We compared each of our 3D models (hereafter denoted as <3D>, obtained from the mean temperature

and pressure structure of the full 3D model), to a corresponding standard hydrostatic 1D model atmosphere (hereafter denoted as 1D<sub>LHD</sub>). The <3D> model is a temporal and horizontal average of the 3D structure over surfaces of equal (Rosseland) optical depth. It is only dependent on the particular way the 3D model is averaged.

The 1D<sub>LHD</sub> model is calculated with a 1D atmosphere code called LHD. It assumes plane-parallel geometry and employs the same micro-physics (equation-of-state, opacities) as CO<sup>5</sup>BOLD. Convection is described by mixing-length theory. Somewhat arbitrary choices to be made relate to the value of the mixing-length parameter, which formulation of mixing-length theory to use, and how turbulent pressure is treated in the momentum equation; see Caffau et al. (2007) for further details. As usual, in the spectral synthesis of the 1D models a value of the micro-turbulence has to be adopted. For 1D as well as 3D models the spectral synthesis calculations were performed with the spectrum synthesis code Linfor3D<sup>2</sup>.

### 4.3. 3D corrections

There are two main effects that distinguish 3D from 1D models, the average temperature profile and the horizontal temperature fluctuations. We quantify the contribution of both effects by introducing the 3D correction as:  $3\text{D} - 1\text{D}_{\text{LHD}}$ .

The average temperature profile provided by a hydrodynamical simulation is different from that of a 1D atmosphere assuming radiative equilibrium. This effect is shown in Fig. 2, where the 3D average temperature profile, plotted as a function of the pressure, is compared to the profiles from 1D<sub>LHD</sub> and MARCS models. As evident from the plot, the <3D> temperature profile is cooler than both 1D models in the outer photospheric layers for both of the stars. This often-encountered effect in metal-poor atmospheres (Asplund et al. 1999) is particularly important for the oxygen abundances derived from OH molecules, as the difference is largest precisely in the layers where these lines are formed. The result is that the oxygen abundances become lower in the 3D formulation than in the 1D; we quantify this effect through the 3D correction as defined above.

## 5. Chemical analysis

### 5.1. Stellar parameters

The atmospheric parameters of each star in the CS 22876–032 system were estimated from the photometric data available in Norris et al. (1993) and Preston et al. (1991), from whom we adopt  $V = 12.84$ ,  $B - V = 0.397$ ,  $U - B = -0.255$  with uncertainties of 0.01, 0.02 and 0.01 respectively. We adopt  $E(B - V) = 0.00 \pm 0.01$  from Norris, Beers, & Ryan (2000) and Schuster et al. (1993, 1996). We also extracted, from the 2MASS<sup>3</sup> database,  $K = 11.503 \pm 0.035$  and  $J = 11.800 \pm 0.041$ . The equations derived by Carpenter (2001) to transform from 2MASS magnitudes to the homogenised photometric system of Bessell & Brett (1988) were then applied.

From the above information it is possible to estimate the reddening-corrected colours  $(U - B)_0$ ,  $(B - V)_0$ ,  $(V - K)_0$  and

<sup>2</sup> more information on Linfor3D can be found in the following link: [http://www.aip.de/~mst/Linfor3D/linfor\\_3D\\_manual.pdf](http://www.aip.de/~mst/Linfor3D/linfor_3D_manual.pdf)

<sup>3</sup> The Two Micron All Sky Survey is a joint project of the University of Massachusetts and the Infrared Processing and Analysis Center/California Institute of Technology, funded by the National Aeronautics and Space Administration and the National Science Foundation.

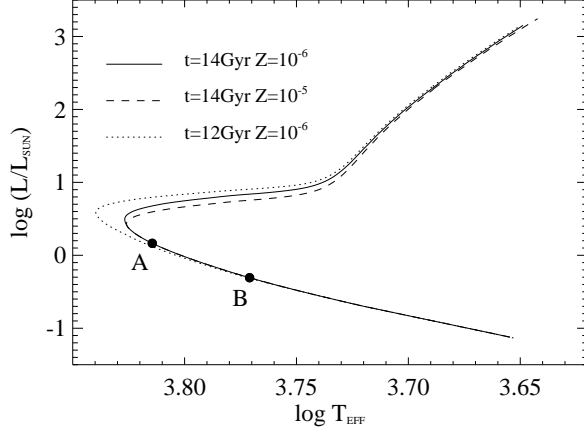


**Fig. 3.** The two components of CS 22876–032 on a 14-Gyr isochrone by Chieffi & Limongi (priv. comm.) for  $Z = 10^{-6}$  (solid line). For comparison, isochrones for 14 Gyr and  $Z = 10^{-5}$  (dashed) and 12 Gyr and  $Z = 10^{-6}$  (dotted) are also shown.

$(J - K)_0$ , which we use to derive the parameters of both components of the binary by comparing with theoretical isochrones. We have chosen the isochrone of Chieffi & Limongi (private communication) for 14 Gyr and metallicity  $Z = 10^{-6}$ , from which one can compute composite colours from pairs of two models that lie on that isochrone. Thus, the stellar parameters can be derived from the best fit to the observed colours that also satisfy the mass ratio determined from the orbital solution.

We note that the isochrones of Chieffi & Limongi use the colour transformations based on ATLAS model atmospheres, for this temperature range, and the synthetic colours of Bessell, Castelli & Plez (1998).

The result is shown in Fig. 3, which corresponds to a primary star with  $T_{\text{eff},A} = 6500$  K and  $\log g_A = 4.4$  and a secondary star with  $T_{\text{eff},B} = 5900$  K and  $\log g_B = 4.6$ . We checked that a change of  $\Delta \text{Age} = -2$  Gyr translates into a change of  $+25$  K and  $-0.01$  dex for the  $T_{\text{eff},A,B}$  and  $\log g_{A,B}$  respectively, whereas a variation of the metallicity of  $\Delta \log Z = +1$  dex does not have any impact on the resulting stellar parameters (see Fig. 3).

The uncertainties of the stellar parameters were estimated using Monte Carlo techniques. We injected noise in the seven observed quantities,  $V, B-V, U-B, K, J, E(B-V)$ , and  $M_B/M_A$  following Gaussian distributions with standard deviations equal to the errors of these quantities. From these distributions we computed a set of five variables,  $(U-B)_0, (B-V)_0, (V-K)_0, (J-K)_0$ , and  $M_B/M_A$  for the 10,000 samples. Then we found the best fit to each of these set of variables via a  $\chi^2$  minimisation, defining  $\chi^2 = \sum_{i=1}^5 (f_{i,\text{obs}} - f_{i,\text{mod}})^2$ ,  $f_{i,\text{obs}}$  being the “observed” value for each Monte Carlo simulation and  $f_{i,\text{mod}}$  the value extracted from two pairs of points in the theoretical isochrone.

The results of these simulations for the effective temperature and surface gravity of both components are shown in Figs. 4 and 5 respectively. The lowest contour encloses roughly 95.4% of the 10,000 Monte Carlo events, analogous to  $2\sigma$  for a normal distribution. From these simulations we adopted an error, at the  $2\sigma$  level, of  $\Delta T_{\text{eff},A} = 100$  K and  $\Delta T_{\text{eff},B} = 150$  K for the effective temperature, and  $\Delta \log g_{A,B} = 0.1$  dex for the surface gravity.

For single stars, the wings of  $H\alpha$  is also a very good temperature indicator (Cayrel 1988; Fuhrmann et al. 1993; van’t Veer-Menneret & Mégessier 1996; Barklem et al. 2002). Adopting the broadening theory of Barklem et al. (2000), we

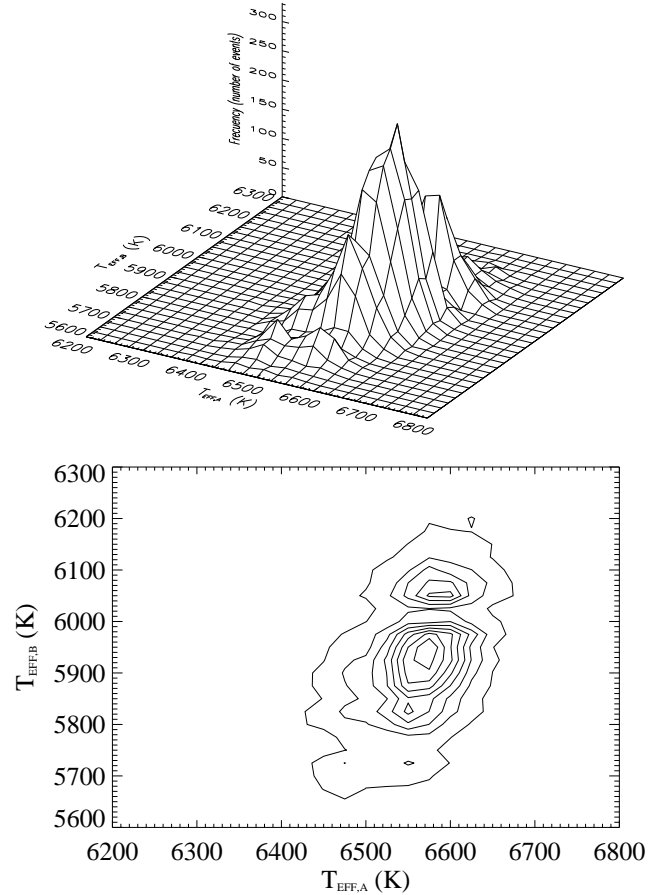


**Fig. 4.** Distribution of effective temperatures for CS 22876–032 A and B obtained by Monte Carlo simulations, comparing the observed colours with those from the isochrone in Fig. 3 for the observed mass ratio. The lowest contour encloses 95.4% of the 10,000 simulations.

computed  $H\alpha$  profiles for several effective temperatures, using TURBOSPECTRUM. Unfortunately, all our UVES spectra were obtained near maximum line separation, and the velocity difference is of the order of  $\sim 30 \text{ km s}^{-1}$ , which precludes separation of the individual  $H\alpha$  profiles. Therefore, we had to compute a composite spectrum in order to match the observed profile.

Fig. 6 compares this synthetic  $H\alpha$  profile with the observed profile for several combinations of effective temperatures  $T_{\text{eff},A} + T_{\text{eff},B}$ . We did not vary  $T_{\text{eff},B}$  because the  $H\alpha$  absorption line of the cooler star B is weaker and severely veiled by the flux of star A, so the combined profile is not sensitive to changes in  $T_{\text{eff},B}$ . This comparison seems to confirm our estimate of the effective temperature from the colours, suggesting as well that it is on the same scale as the  $H\alpha$ -based temperatures.

## 5.2. Stellar elemental abundances

Most of the elemental abundances were determined from equivalent width measurements of selected unblended lines. These were made with an automatic line-fitting procedure based on the algorithms of Charbonneau (1995), which performs both line detection and gaussian fits to unblended lines. The implementation is the same as described in François et al. (2003). The equivalent widths were then corrected for the appropriate veiling factors and provided as input to TURBOSPECTRUM to determine

**Table 3.** Element abundances of CS 22876-032. The Solar O abundance is adopted from the 3D measurement of atomic lines of Ludwig & Steffen (2007); the other Solar abundances from Grevesse & Sauval (2000).  $[X/H]$  and  $[X/Fe]$  are LTE values;  $[X/Fe]$  refers to Fe I for OH and neutral species, to Fe II for ionised species. The 3D abundance corrections  $\Delta_{3D-1D}$  were determined with TURBOSPECTRUM from the  $\langle 3D \rangle$  and 1D models, except for O and Li, where a full 3D analysis was performed and we give two values: The abundance correction  $3D - \langle 3D \rangle$  (“ $\langle 3D \rangle$ ”) and “ $1D$ ” =  $3D - 1D_{LHD}$  (see text).  $\sigma$  is the standard deviation of the results from the  $n$  lines (next column; if  $n = 1$ , the wavelength of the line in nm is given). See text for details on the measurement of Li, O, Sc, and Co.

Species	$\log \epsilon(X)_\odot$	$[X/H]_A$	$[X/Fe]_A$	$\Delta_{3D-1D,A}$	$\sigma_A$	$n_A$	$[X/H]_B$	$[X/Fe]_B$	$\Delta_{3D-1D,B}$	$\sigma_B$	$n_B$
Li I	–	2.22	–	$\langle 3D \rangle: -0.17$ $1D: -0.19$	0.01	670.8	1.75	–	$\langle 3D \rangle: -0.02$ $1D: -0.29$	0.04	670.8
O (OH)	8.72	-1.52	2.14	$\langle 3D \rangle: -0.64$ $1D: -1.49$	0.04	4	-1.75	1.81	$\langle 3D \rangle: 0.00$ $1D: -0.92$	0.09	9
Na I	6.33	-3.69	-0.03	-0.01	0.03	2	-3.79	-0.22	0.02	0.05	589.5
Mg I	7.58	-3.11	0.55	0	0.18	9	-3.14	0.43	0.09	0.24	9
Al I	6.47	-3.89	-0.23	-0.02	0.22	2	-3.75	-0.18	0.04	0.22	2
Si I	7.55	-3.75	-0.09	-0.01	0.02	390.5	-3.48	0.09	0.07	0.04	390.5
Ca I	6.36	-3.65	0.01	-0.07	0.02	422.6	-3.68	-0.11	-0.04	0.04	422.6
Ca II	6.36	-3.68	-0.18	0.10	0.14	3	-3.81	-0.54	0.23	0.11	2
Sc II	3.17	-3.73	-0.22	0	0.18	2	-3.57	-0.30	0.04	0.11	2
Ti II	5.02	-3.25	0.25	-0.01	0.34	19	-3.45	-0.18	0.09	0.23	12
Cr I	5.67	-3.79	-0.13	-0.07	0.12	5	-3.92	-0.35	-0.08	0.35	4
Cr II	5.67	-3.38	0.12	0.08	0.10	313.2	-3.30	-0.03	0.24	0.30	313.2
Mn II	5.39	-4.01	-0.51	0.09	0.17	344.1	-3.86	-0.59	0.14	0.37	344.1
Fe I	7.50	-3.66	0	-0.12	0.12	38	-3.57	0	-0.07	0.21	37
Fe II	7.50	-3.51	0	0.09	0.25	13	-3.27	0	0.18	0.31	9
Co I	4.92	-2.91	0.75	-0.13	0.07	7	-2.92	0.65	-0.07	0.08	4
Ni I	6.25	-3.49	0.17	-0.19	0.18	12	-3.45	0.12	-0.08	0.16	12

**Table 4.** Abundance errors in CS 22876–032.  $\Delta_{T_{\text{eff}}}$ ,  $\Delta_{\log g}$ , and  $\Delta_\xi$  are the abundance changes caused by changes in  $T_{\text{eff}}$  of 100K (A) or 150K (B), in  $\log g$  by 0.1 dex, and by 0.5 km s<sup>−1</sup> in the microturbulence velocity  $\xi$ . Other column headings and comments as in Table 3.

Specie	$\log \epsilon(X)_\odot$	$[X/H]_A$	$\Delta_{A,T_{\text{eff}}}$	$\Delta_{A,\log g}$	$\Delta_{A,\xi}$	$n_A$	$[X/H]_B$	$\Delta_{B,T_{\text{eff}}}$	$\Delta_{B,\log g}$	$\Delta_{B,\xi}$	$n_B$
Li I	–	2.22	0.06	0	0	670.8	1.75	0.08	0	0	670.8
O (OH)	8.72	-1.52	0.13	-0.04	0.01	4	-1.75	0.23	0.02	0.04	9
Na I	6.33	-3.69	0.05	0	-0.01	2	-3.79	0.07	0	-0.01	589.5
Mg I	7.58	-3.11	0.04	0	-0.05	9	-3.14	0.04	0	-0.04	9
Al I	6.47	-3.89	0.06	0	-0.01	2	-3.75	0.06	0.02	-0.03	2
Si I	7.55	-3.75	0.06	0.01	-0.01	390.5	-3.48	0.04	0.02	-0.05	390.5
Ca I	6.36	-3.65	0.06	0	-0.06	422.6	-3.68	0.04	0.01	-0.11	422.6
Ca II	6.36	-3.68	0.01	0.03	-0.06	3	-3.81	-0.05	0.05	-0.06	2
Sc II	3.17	-3.73	0.04	0.03	-0.01	2	-3.57	0.04	0.05	-0.01	2
Ti II	5.02	-3.25	0.05	0.03	-0.04	19	-3.45	0.01	0.05	-0.09	12
Cr I	5.67	-3.79	0.08	0	-0.01	5	-3.92	0.10	0.02	-0.02	4
Cr II	5.67	-3.38	0.03	0.03	-0.07	313.2	-3.30	-0.05	0.05	-0.08	313.2
Mn II	5.39	-4.01	0.04	0.03	-0.01	344.1	-3.86	-0.14	0.04	-0.01	344.1
Fe I	7.50	-3.66	0.09	-0.01	-0.05	38	-3.57	0.06	-0.02	-0.12	37
Fe II	7.50	-3.51	0.03	0.02	-0.02	13	-3.27	-0.02	0.03	-0.06	9
Co I	4.92	-2.91	0.09	0	-0.01	7	-2.92	0.09	0.01	-0.07	4
Ni I	6.25	-3.49	0.09	0	-0.05	12	-3.45	0.07	0.01	-0.13	12

the abundances. The detailed line-by-line abundances, together with observed EWs, veiling factors, and atomic data for both components can be found in Table A.1.

The mean abundances for each element, listed in Table 3, are computed using the adopted stellar parameters derived in § 5.1 and a microturbulence of  $\xi_t = 1.5$  km s<sup>−1</sup>. We have only performed full 3D computations with Linfor3D for the Li doublet and the OH lines. A full 3D analysis for the hundreds of lines involved in this work is a considerable computational task, well beyond the scope of the present paper. However, we used the  $\langle 3D \rangle$  models as input to TURBOSPECTRUM to estimate the expected corrections due to the different average temperature profiles of the 3D models. From the full 3D spectrum synthesis performed for Li and OH, we expect this to be close to the *true* 3D correction for star B, while we expect significant contributions from

the temperature fluctuations in star A. In the following we refer to  $(\langle 3D \rangle - 1D_{\text{MARCS}})$  to represent the difference between the abundance found by TURBOSPECTRUM using a  $\langle 3D \rangle$  model and that found using a MARCS 1D model. This is to distinguish them from the *true* 3D corrections.

### 5.2.1. Veiling corrections

In a double-lined spectrum the strength of each spectral line, in particular those of the fainter component, is reduced by veiling from the continuum flux of the other star. Thus, the measured equivalent widths for each spectral component must be corrected for this veiling effect, in order to obtain the intrinsic values. The corrected equivalent widths can be estimated by multiplying the observed EWs by veiling factors,  $f_{\lambda,i}$ , which solve the equation

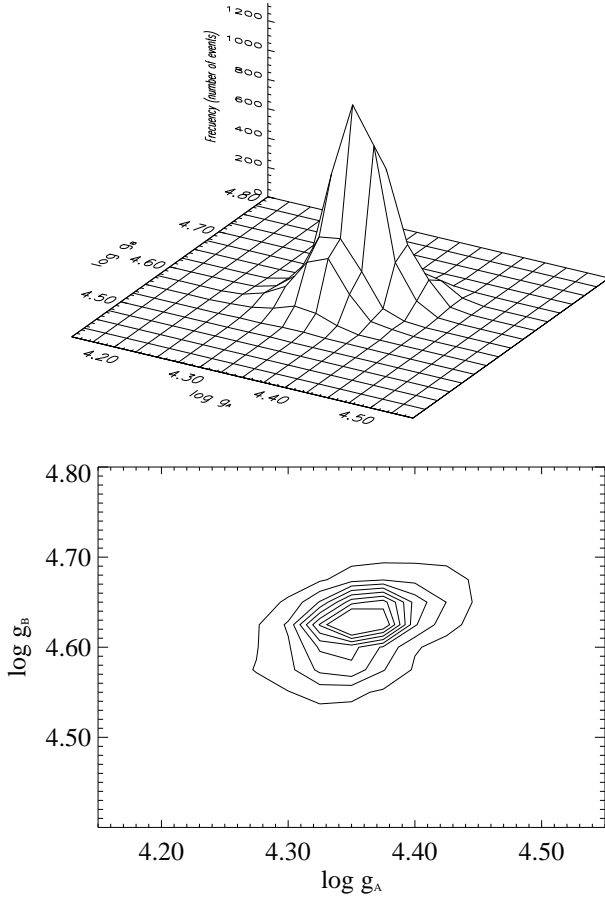


**Fig. 5.** Same as Fig. 4, for the surface gravities.

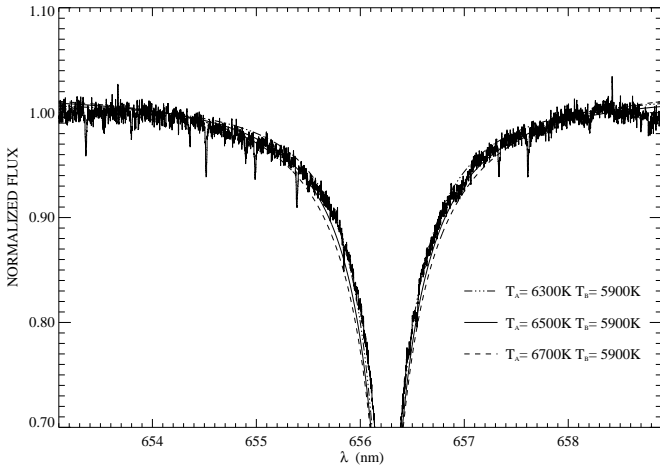


**Fig. 6.** Computed  $H_\alpha$  profiles for three sets of effective temperatures, 6300+5900, 6500+5900 and 6700+5900, and normalised to the level of the observed UVES spectrum at 645.0 nm.

$1/f_{\lambda,A} + 1/f_{\lambda,B} = 1.0$  and where  $f_{\lambda,B}/f_{\lambda,A}$  is the primary-to-secondary luminosity ratio. The values  $f_{\lambda,i}$  are wavelength dependent and can be estimated theoretically by computing the flux of each stellar component, taking into account the ratio of the stellar radii. Thus, the luminosity ratio can be expressed as  $f_{\lambda,B}/f_{\lambda,A} = F_{\lambda,A}/F_{\lambda,B} \times (R_A/R_B)^2$ , where  $F_{\lambda,i}$  and  $R_i$  are the flux and radius of each star.

For consistency with the isochrone colours, we use version 9 of the ATLAS code (Kurucz 1993a, 2005a) in its Linux version (Sbordone et al. 2004; Sbordone 2005) to compute model atmospheres and fluxes for each star by adopting the  $T_{\text{eff}}$  and  $\log g$  derived in § 5.1. We used the “NEW” Opacity Distribution Functions (Castelli & Kurucz 2003), with  $1 \text{ km s}^{-1}$  microturbulence, a mixing-length parameter  $\alpha_{\text{MLT}}$  of 1.25, and no overshooting. The formulation of the mixing length is different between MARCS and ATLAS; that used in our MARCS models roughly corresponds to  $\alpha_{\text{MLT}} \sim 1.1$  in the ATLAS formulation.

The veiling factors thus computed differ from the MARCS+TURBOSPECTRUM ones on average by 0.02 which, for a line on the linear part of the curve of growth, translates into a difference in abundance of 0.009 dex, which is negligible within the accuracy of our analysis. This allowed us to compute quickly veiling factors for different combinations of the parameters of the two stars, which were then used to estimate the associated uncertainties. For consistency, we used the ATLAS veiling factors throughout.

The ratio of the stellar radii was extracted from the theoretical isochrone, being  $R_A/R_B = 1.4$ . The derived veiling factors lie in the range  $f_{\lambda,A} = 1.29 - 1.37$  ( $f_{\lambda,B} = 4.47 - 3.70$ ) in the spectral region  $\lambda\lambda 300.0-700.0 \text{ nm}$ . These estimates also compare well with those used by Norris, Beers, & Ryan (2000), although they adopted fixed values for large spectral regions. In particular, they used  $f_{\lambda,A} = 1.28$  and  $f_{\lambda,B} = 4.60$  for all Fe lines between 370 and 440 nm, whereas we used  $f_{\lambda,A} = 1.28 - 1.31$  and  $f_{\lambda,B} = 4.19 - 4.58$  in that spectral region (see Table A.1).

In addition to the 1D veiling factors computed for the effective temperatures of both stars, we also calculated the (3D) veiling factors using the (3D) atmospheric models (whose temperature structure is different from that of the OSMARCS 1D models). These veiling factors were adopted to properly correct the EWs given as input to the TURBOSPECTRUM code to estimate the ((3D) – 1D<sub>MARCS</sub>) abundance corrections (see § 5.2). In addition, we note that the 3D – 1D<sub>LHD</sub> correction (see § 4.2), computed only for Li and OH lines, does not consider different veiling factors for 1D and 3D models. In this case, we computed only the 3D veiling factors using the continuum flux provided by the full 3D model of each star in the spectral region close to these lines. Thus, these 3D veiling factors were applied to the observed EWs, and the resulting EWs were used to compute the 3D – 1D<sub>LHD</sub> corrections reported in Table 3.

### 5.2.2. Uncertainties in the abundance analysis

The abundance measurements are dependent on the model parameters, i.e. effective temperature, surface gravity and microturbulence. However, in the analysis of a spectroscopic binary, it is not possible to avoid the influence of the veiling factors on the error estimates. The veiling factors depend on the effective temperatures and surface gravities of both stars. Therefore, in order to estimate the sensitivity of an element’s abundance to a given stellar parameter, one should also estimate how veiling factors change when one of the stellar parameters of each star is modified. Thus, we have also computed 1D veiling factors for four pairs of models  $T_{\text{eff,A}}/\log g_A$ ,  $T_{\text{eff,B}}/\log g_B$  according to the errors of the stellar parameters (see § 5.1), by changing one stellar parameter and fixing the three remaining parameters. The uncertainties on the elemental abundances due to the errors of the different model parameters are listed in Table 4. The uncertainty of the microturbulence was assumed to be  $0.5 \text{ km s}^{-1}$ .

The errors computed from the dispersion of the line measurements and the signal-to-noise ratios are listed in Table 3.

**Table 5.** Li abundances in CS 22876-032.  $A(\text{Li})_{1\text{D,NLTE,DC}}$  includes corrections for depletion by diffusion (see text).

Component	$\text{EW}_{\text{obs}}$ (pm)	$f_{6708,1\text{D}}$	$A(\text{Li})_{1\text{D}}$	$A(\text{Li})_{1\text{D,NLTE}}$	$A(\text{Li})_{1\text{D,NLTE,DC}}$	$\Delta_{3\text{D}-(3\text{D})}$	$\Delta_{3\text{D}-1\text{D}}$
Star A	1.32	1.36	2.22	2.18	2.18	-0.17	-0.19
Star B	0.42	3.74	1.75	1.77	1.84	-0.02	-0.29

We used the Cayrel formula (Cayrel 1988) to estimate the errors of the observed EWs. Due to the high S/N of the spectra we have obtained, these errors are typically  $\lesssim 0.1$  pm in most of the spectral region covered, except for the blue spectrum at 310.0–320.0 nm where the S/N ratio drops significantly. Thus, the dispersion of the measurements for elements with lines in this range is larger than for lines above 400 nm. In Table 3, we give the larger of these two estimates for each element in each star. For Li, the error due to the uncertainty in the continuum level has been computed from a Monte Carlo simulation, by injecting noise corresponding to the actual S/N ratio near the Li line in the best-fit synthetic spectrum. In each case, the S/N ratio was estimated taking into account the corresponding veiling factors.

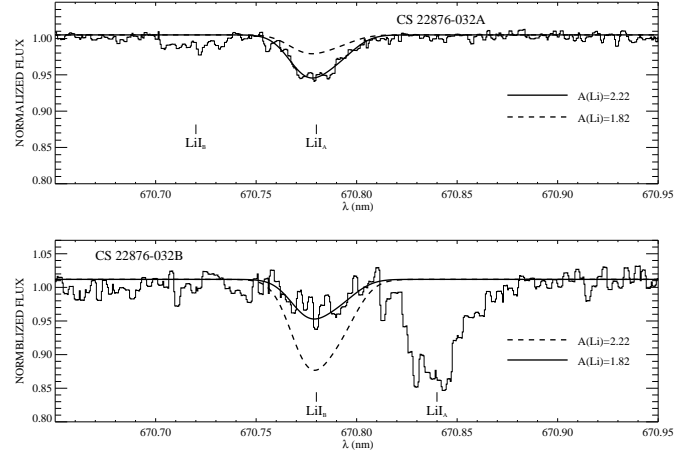
### 5.2.3. The iron abundance

We made a careful selection of 38 reliable Fe I lines in star A and 37 in B, taking into account the radial velocity separation of the two sets of lines in the double-lined spectrum. It is reassuring that we find the same  $[\text{Fe}/\text{H}]$  for both stars, within the errors. Note that in our analysis, in contrast with Norris, Beers, & Ryan (2000), this was not imposed *a priori*, and thus supports our determination of atmospheric parameters. Our value of  $[\text{Fe}/\text{H}]$  is very close to that by Norris, Beers, & Ryan (2000) despite the very different effective temperatures adopted. This results from the fact that different effective temperatures also imply different veiling factors, which must be factored in.

Reviewing the  $\langle 3\text{D} \rangle - 1\text{D}_{\text{MARCS}}$  corrections, we see that  $[\text{Fe}/\text{H}]$  is reduced in 3D, and the difference between the two stars increases. We expect the true 3D corrections of the primary star to be largely due to horizontal temperature fluctuations, therefore probably larger than our  $\langle 3\text{D} \rangle - 1\text{D}_{\text{MARCS}}$  correction, and we predict that a full 3D-LTE synthesis will not improve the agreement of  $[\text{Fe}/\text{H}]$  between the two stars. Our best estimate of  $[\text{Fe}/\text{H}]$  of the system is still the  $\langle 3\text{D} \rangle - 1\text{D}_{\text{MARCS}}$  corrected value for star A:  $[\text{Fe}/\text{H}] = -3.78$ , which might be further reduced by a full 3D-LTE synthesis. This confirms that the stars in CS 22876–032 are the most metal-poor dwarfs known to date.

We note that ionisation equilibrium is not achieved in either star. In both, the abundance derived from the Fe II lines is larger, for star B by a factor of two. We note, however, that the Fe II abundance shows a very large scatter in both A and B (0.25 and 0.31 dex, respectively) so that, within errors, the Fe I and Fe II abundances remain compatible. The number of Fe II lines measured is very large for stars of this metallicity (13 in star A, 9 in B). However, all the Fe II lines are weak and the majority of them are in the UV range, where the S/N ratio of our spectra drops dramatically.

The  $\langle 3\text{D} \rangle - 1\text{D}_{\text{MARCS}}$  corrections for Fe II are in the *opposite* direction of those for Fe I, making the ionisation imbalance worse. The different signs of the  $\langle 3\text{D} \rangle - 1\text{D}_{\text{MARCS}}$  corrections for neutral and ionised species are due to the different ionisation structure of the  $\langle 3\text{D} \rangle$  and 1D models. We note that for the

**Fig. 7.** Synthetic spectral fits to the Li line in the co-added UVES spectrum of star A (top) and B (bottom). The observed spectra have been corrected for veiling (see Table 5), so the lines appear with their intrinsic strength in each star.

metal-poor subgiant HD 140283, Shchukina et al. (2005) have performed NLTE computations for Fe I and Fe II, using a single snapshot of a hydrodynamical simulation, and found 3D-NLTE corrections of +0.6 for Fe I and +0.4 for Fe II. To the extent that these computations can be considered representative of the stars in CS 22876–032, we expect that a full 3D-NLTE analysis might achieve a better ionisation balance for iron.

### 5.2.4. Lithium

The high quality of our spectra allowed us to measure the Li doublet in both components of CS 22876-032 for the first time. Fig. 7 shows our mean spectra of the Li region, where our well-resolved spectra (only) have been co-aligned on the lines of star A (top) and B (bottom), respectively. The superposed lines of the other star appear only slightly diffuse, because the velocity difference between the two stars is nearly the same in all our UVES spectra (see Table 1). The spectra in Fig. 7 have been corrected for veiling, as discussed in § 5.2.1.

The Li abundance of each star was computed from two sets of spectra taken on different nights. We found differences of 0.01 and 0.05 dex between star A and B and adopted the average value of the two measurements. Table 5 lists the observed equivalent widths and the average Li abundances, with and without the NLTE corrections obtained from the tables of Carlsson et al. (1994). We further correct for the effect of depletion as predicted by the standard isochrones of Deliyannis, Demarque, & Kawaler (1990). The correction is negligible for the hot primary, but larger for the secondary (see Table 5).



It is certainly surprising that the two components appear to have a different lithium content. The Li abundance of the primary component seems to be consistent with that observed in other metal-poor stars, i.e., the *Spite plateau* (Spite & Spite 1982a,b; Bonifacio & Molaro 1997; Ryan, Norris, & Beers 1999; Meléndez & Ramírez 2004; Charbonnel & Primas 2005; Asplund et al. 2006; Bonifacio et al. 2007), modulo the uncertainties on the temperature scales adopted over the years by the various authors, but the secondary star definitely seems to exhibit a lower Li content.

According to the Li depletion isochrones of Deliyannis, Demarque, & Kawaler (1990), if star B were 350 K cooler than we assume, the correction for  $A(\text{Li})$  would be 0.6 dex. Such a change in  $T_{\text{eff}}$  would also imply a slightly higher  $\log g$  from the isochrone, so the model dependencies given in Table 4 would imply that  $A(\text{Li})$  should be reduced by 0.17, giving a “corrected” Li abundance of  $A(\text{Li})=2.20$ , in essential agreement with  $A(\text{Li})$  of the primary (we do not consider variations in the temperature of star A). By changing simultaneously the effective temperatures of the pair (within the range allowed by photometry), we would derive different Li abundances for each of the components. However, we would also change the veiling factors, and the final abundance difference between the two stars would be roughly the same.

We have checked whether inaccurate veiling corrections, especially for the fainter lines of star B, could be the cause of the different Li abundances. It turns out that this is impossible: bringing  $A(\text{Li})_B$  into consistency with the *Spite plateau* would require a doubling of the veiling correction at 670 nm; given that we find consistent abundances for Na at 590 nm and Mg I at 880 nm, the veiling correction cannot be off by a factor two at the intermediate wavelength.

For the Li lines we also performed a full 3D-LTE synthesis using Linfor3D. The resulting corrections are listed in Table 5. Since the 3D computation was performed in LTE, the Li abundances must not be taken as definitive, as shown by Cayrel & Steffen (2000) and Asplund et al. (2003). It is, however, interesting to notice that while the 3D effect in star A is almost entirely due to the horizontal temperature fluctuations, for star B it is almost entirely due to the cooler average temperature profile of the 3D model. A full 3D-NLTE synthesis of Li in CS 22876–032 is beyond the scope of this paper. Full 3D-NLTE synthesis of the Li profile in HD74000 have been addressed recently by Cayrel et al. (2007).

### 5.2.5. Oxygen

The oxygen abundances have been derived from UV OH lines of the (0-0) vibrational band of the  $A^2\Sigma - X^2\Pi$  electronic system. The use of these lines for oxygen measurements in metal-poor stars was pioneered by Bessell et al. (1991). We were able to measure four lines in the primary and nine lines in the secondary. Following the extensive surveys of OH lines in metal-poor stars by Israelian et al. (1998); Boesgaard et al. (1999); Israelian et al. (2001), and the controversial finding of strongly increasing  $[\text{O}/\text{Fe}]$  with decreasing metallicity, Asplund & García Pérez (2001) warned of the possible role of 3D effects on the formation of these lines. For this reason we decided to compute *ad hoc* CO<sup>5</sup>BOLD hydrodynamical simulations for this system in order to correctly evaluate the 3D effects. Our results are summarised in Table 6. Some of the analysed lines are shown in Figs. 8, 9 and 10.

The 3D effects are clearly large and considerably different between the two stars. Asplund & García Pérez (2001) at-

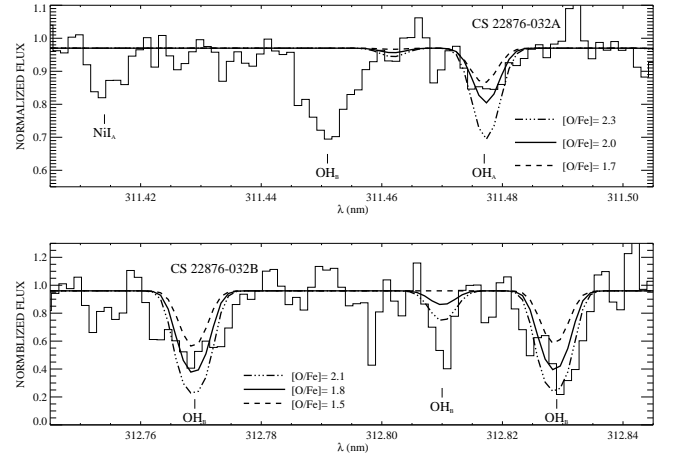


**Fig. 8.** Synthetic spectral fits to OH lines in the co-added UVES spectrum of star A (top) and B (bottom) in CS 22876–032. The observed spectra have been corrected for veiling factors of 1.30 (A) and 4.36 (B).

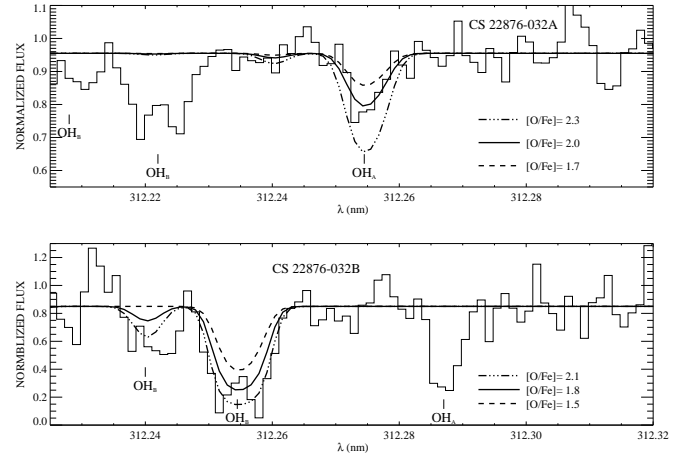


**Fig. 9.** Same as Fig. 8 for another OH line.

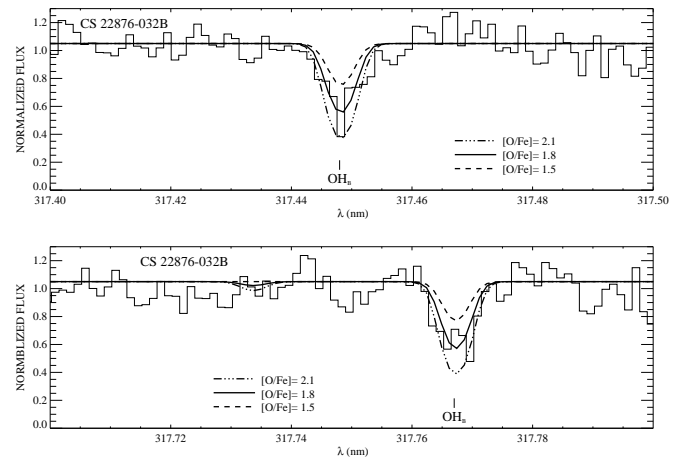


**Fig. 10.** Synthetic spectral fits to OH lines in the co-added UVES spectrum of star B. The observed spectra have been corrected for a veiling factor of 4.36.

**Table 6.** 3D abundance corrections for the OH lines. [O/H] and [O/Fe] are relative to  $\log \epsilon(\text{O})_{\odot} = 8.72$ .

$\lambda$ (nm)	[O/H] <sub>1D</sub> <sup>a</sup>	[O/Fe] <sub>1D</sub>	$\Delta_{3\text{D}-(3\text{D})}$	$\Delta_{3\text{D}-1\text{D}}$
CS 22876–032A				
311.21	-1.48	2.18	-0.633	-1.546
311.47	-1.55	2.11	-0.536	-1.328
312.26	-1.56	2.10	-0.590	-1.420
313.43	-1.48	2.18	-0.797	-1.664
CS 22876–032B				
312.26	-1.63	1.94	0.027	-0.985
312.77	-1.85	1.72	0.014	-0.868
312.83	-1.68	1.89	0.033	-1.009
313.03	-1.94	1.63	-0.004	-1.045
313.32	-1.69	1.88	0.003	-0.856
313.66	-1.75	1.82	-0.015	-0.849
314.30	-1.80	1.77	-0.011	-0.815
317.45	-1.75	1.82	-0.017	-0.916
317.77	-1.70	1.87	-0.009	-0.906

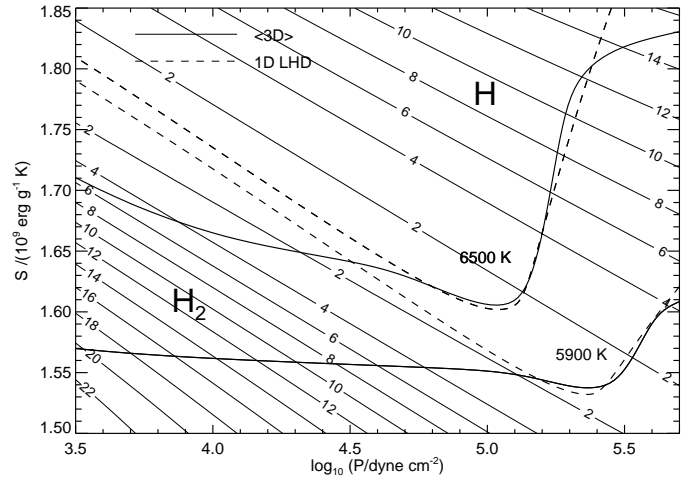
**Table 7.** 1D gravity effects on the Fe and O abundances

Species	$\Delta \log g$	$\Delta[\text{X}/\text{H}]_A$	$\Delta[\text{X}/\text{H}]_B$
OH	0.3	-0.12	-0.08
Fe I	0.3	-0.01	-0.02
Fe II	0.3	0.09	0.11

tributed the 3D corrections primarily to the different average temperature profile of the 3D models, in particular to their extremely cool outer layers. However, we see that for the primary star the 3D correction is almost evenly shared between average temperature profile and horizontal temperature fluctuations<sup>4</sup>.

Our cooler 3D model atmosphere exhibits much smaller temperature fluctuations around the mean than the hotter one. In the cool component the average temperature becomes so low that a substantial amount of  $\text{H}_2$  is formed in the higher photospheric layers. The associated increase of the specific heat makes it much harder for pressure fluctuations to introduce temperature fluctuations. Due to the smaller temperature fluctuations the cooler 3D and  $\langle 3\text{D} \rangle$  models provide essentially the same abundances. The model of the primary star is hotter on average,  $\text{H}_2$  molecules are much less abundant, and temperature fluctuations are much more pronounced. Consequently, the resulting abundances differ between 3D and  $\langle 3\text{D} \rangle$  models.

Fig. 11 illustrates the situation. The 3D model exhibits a stronger cooling with respect to the  $1\text{D}_{\text{LHD}}$  model at 5900 K than is the case at 6500 K. Over a wide pressure range the structure is almost adiabatic and passes through a region of substantial  $\text{H}_2$  molecule formation, indicated by the rather high values of the specific heat, suppressing temperature fluctuations in that region. The almost adiabatic structure of the cool model also indicates that the convective overshooting is very efficient compared to radiative heating, and has driven the thermal structure into almost adiabatic equilibrium.

**Fig. 11.** Entropy profiles of the  $\langle 3\text{D} \rangle$  CO<sup>5</sup>BOLD model atmospheres (solid lines), compared to  $1\text{D}_{\text{LHD}}$  models (dashed lines) for stars B (5900 K) and A (6500 K). The labelled contours indicate the specific heat at constant pressure in units of  $10^8 \text{ erg g}^{-1} \text{ K}^{-1}$  (see text).

The large difference in the behaviour of our two models warns us that to measure reliable abundances from OH one needs a grid of 3D models which is fairly dense in temperature, to capture, for any metallicity, the  $T_{\text{eff}}$  at which  $\text{H}_2$  formation sets in.

Finally, we note that the O abundance derived from OH lines is rather sensitive to the surface gravity, as can be seen from Table 7. An increase of gravity of 0.3 dex introduces a decrease in O abundance of about 0.1 dex. This gravity dependence is larger than that of Fe I, however it is advisable to use Fe I to derive [O/Fe], since the gravity dependence of Fe II is in the *opposite* direction. Note that the values reported in Table 7 have been estimated without revising the veiling factor when changing the surface gravity of the models, contrary to the error estimates described in § 5.2.2.

#### 5.2.6. Other elements

The Be II resonance doublet at 313.0 nm is within the wavelength range covered by our spectra. The S/N ratio in that region is  $\sim 25$ , yet none of the Be lines is detected, which implies an upper limit for the Be abundance  $\log(\text{Be}/\text{H}) < -13.0$ . As this is an order of magnitude higher than the Be abundance expected for these stars from the trend of Be abundance with metallicity (Gilmore et al. 1992; Ryan et al. 1992; Molaro et al. 1997; Boesgaard et al. 1999; Primas 2002; Boesgaard & Novicki 2006), this result is not of deep significance.

For the other elements, abundances were determined directly from the EWs, except for Sc and Co for which we used spectrum synthesis to take hyperfine splitting (HFS) into account. For Co we used the *A* and *B* factors measured by Pickering (1996). For the Sc II 361.3 nm line we used the *A* and *B* factors measured by Gangrsky et al. (2006). In both cases we used the code `LINESTRUC` of Wahlgren (2005) to compute HFS components. For the Sc II 424.6 nm line we used the HFS components given in Table 5 of McWilliam et al. (1995). The detailed atomic data of HFS for Sc and Co are provided in Table A.2. For Mn we used a single line, the strongest of the Mn II lines of Mult. 3, for which hyperfine splitting is negligible according to Castelli & Hubrig (2004).

<sup>4</sup> -0.64 dex due to temperature fluctuations and -0.85 dex due to average temperature profile

Silicon was only measured from the Si I line at 390.5 nm. In metal-poor cool giants, the silicon abundance is derived from a line at 410.3 nm, since the line Si I 390.5 nm is severely blended with CH lines (Cayrel et al. 2004). The Si I at 410.3 nm is very weak in metal-poor dwarfs, but CH lines are so weak that the line at 390.5 nm can be used.

Aluminium was measured from the resonance lines Al I 394.4 nm and Al I 396.1 nm. The Al I 394.4 nm is blended with CH lines, which are also extremely weak in metal-poor dwarfs and were not taken into account. In fact, we computed synthetic spectra of the CH lines at 390.5 nm and 394.4 nm for the stellar parameters of both dwarfs, and the CH lines are not visible even for  $[C/Fe]$  as large as +2 dex. However, the 394.4 nm line provided a significantly larger abundance than that derived from the 396.1 nm line in both stars. For this reason, in Table 3 we give the average Al abundance derived from both lines with a large dispersion of  $\sim 0.2$  dex.

Using (3D) models, we determine the  $(\langle 3D \rangle - 1D_{\text{MARCS}})$  corrections listed in Table 3. We note that the  $(\langle 3D \rangle - 1D_{\text{MARCS}})$  corrections also take into account different veiling factors estimated using (3D) models and 1D OSMARCS models. In general, the veiling factors estimated from (3D) models are higher for star B and lower for star A than those obtained using 1D models. This effect is especially important for the secondary star, and becomes more significant at shorter wavelengths. Taking into account this effect, it is interesting to note that  $(\langle 3D \rangle - 1D_{\text{MARCS}})$  corrections are in general negative for neutral species and positive for ionised species, at least for the primary star, for which the veiling factors are not significantly different from those estimated using 1D models, as already noted for iron. This reflects the different ionisation structure of 1D and (3D) models. The  $(\langle 3D \rangle - 1D_{\text{MARCS}})$  corrections do not help to achieve ionisation equilibrium for Ca, Cr and Fe, the only elements for which abundances were determined from both neutral and ionised species.

## 6. Discussion

### 6.1. Lithium

In Fig. 12 we show the lithium abundances for the two components of CS 22876–032, together with our data from Paper VII, including the data of Asplund et al. (2006) rescaled in  $[Fe/H]$  and  $A(Li)$  to be homogeneous with our own data. Star A appears to have a Li abundance at the same level as the majority of stars with metallicity below  $-2.5$ , if anything slightly higher. Star B appears to be far below<sup>5</sup> any of the other measured stars. It should be noted that all the other stars in Fig. 12 have effective temperatures determined from the wings of  $H\alpha$  using the broadening theory of Barklem et al. (2000), while for CS 22876–032 they have been determined independently from colours and isochrones. However, the reasonable agreement between our computed  $H\alpha$  profile and the observed profile shown in Fig. 6 suggests that the two temperature scales are fairly close.

The fact that at the lowest observable metallicity, star A remains at the level of the plateau suggests that there is no downturn or decrease in Li abundance at the lowest metallicities. This suggests that the slope of  $A(Li)$  with  $[Fe/H]$  which is detectable in the sample of Asplund et al. (2006) (but not in that of Paper VII, alone) is not real, but rather an artifact due to the  $H\alpha$  temperature scale. It is possible that it is ultimately due to our inability to correctly model the atmospheres of extremely metal-poor

<sup>5</sup> -0.33 dex below the average Li abundance of the stars presented in paper VII

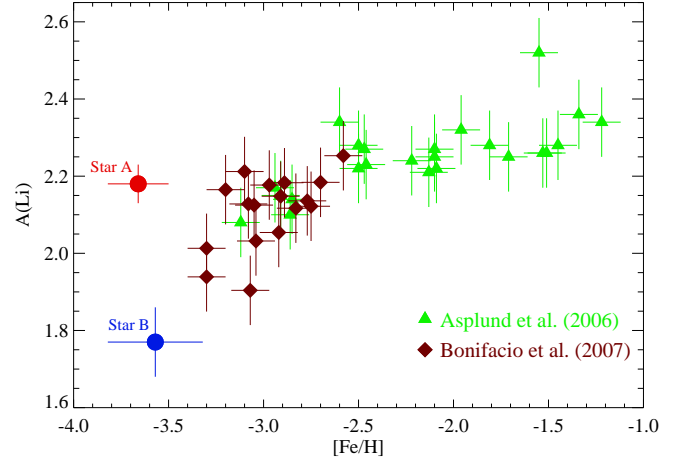


**Fig. 12.** 1D-NLTE Li abundances vs.  $[Fe/H]$  for the stars in CS 22876–032 (circles) and in other metal-poor dwarfs as reported by Asplund et al. (2006, triangles) and Bonifacio et al. (2007, rhombs). The Li abundances by Asplund et al. (2006) were recomputed using TURBOSPECTRUM as reported by Bonifacio et al. (2007). No 3D-LTE or 3D-NLTE has been considered.

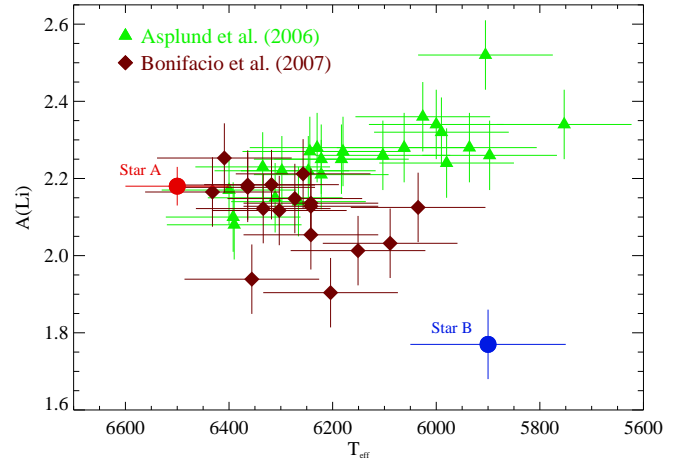


**Fig. 13.** Same as Fig. 12, but in the  $Li-T_{\text{eff}}$  plane.

stars and the wings of Balmer line profiles. In Paper VII we argued that the data could suggest either a vertical drop or an increased scatter in  $A(Li)$  at the lowest metallicities. Now, the drop seems to be ruled out by the  $A(Li)$  measured in star A. The measurement in star B, taken at face value, may support the idea that at metallicities below  $-2.5$ , the *Spite plateau* displays a sizeable scatter.

In section 5.2.4 we have pointed out how the difference of the Li abundance between the two stars could be resolved by assuming that the temperature of star B were 5550 K. Star B would thus be subject to considerable Li depletion, according to the standard Li depletion isochrones of Deliyannis, Demarque, & Kawaler (1990). Such isochrones are available only for metallicities considerably higher than that of CS 22876–032. If, for any reason, either the lower metallicity of our system, or inclusion of other physical phenomena, the dependence of Li depletion on  $T_{\text{eff}}$  is steeper than predicted by purely diffusive standard isochrones, then to reconcile the Li abundances of the two stars, the temperature of star B could be higher than 5550 K. Considering that

our estimated error on the effective temperature of star B is 150 K ( $2\sigma$ ), such cooler temperatures are not totally implausible.

In our view the existence of a real scatter in Li abundances at the lowest metallicities remains to be established beyond any reasonable doubt. It is, nevertheless, worthwhile to discuss the possible implications of such a scatter, if real.

We have already noted in Paper VII that by arbitrarily dividing the sample into two sub-samples, one with metallicity below  $-3.0$  and the other above, the scatter of the “higher” metallicity sample was 0.05 dex, while the scatter of the “lower” metallicity sample was 0.11. If to the lower metallicity sample we add the two stars of CS 22876–032, the scatter increases only slightly, to 0.12 dex. Richard et al. (2005) have studied the effect of atomic diffusion in presence of turbulence and concluded that the observations of the *Spite plateau* could be explained by starting from a primordial A(Li), compatible with the baryonic density derived from the WMAP experiment. The effect of atomic diffusion, countered by a suitably parametrised turbulence, can explain the present level and low scatter of the *Spite plateau*.

From their Li isochrones in the presence of pure atomic diffusion (Fig. 5 of Richard et al. 2005) it is obvious that one should expect Li abundances in the range  $1.70 \leq A(\text{Li}) \leq 2.35$ . The sample constituted by the 8 stars from Paper VII with metallicity below  $-3.0$  and the two stars in CS 22876–032 spans the range 1.91 - 2.20 in A(Li). One could therefore suspect that in extremely metal-poor stars, turbulence is lower and atomic diffusion more efficient, causing the increased scatter in Li abundance. In Fig. 13 we see no clear trend of A(Li) vs.  $T_{\text{eff}}$ . When comparing this figure with Fig. 5 of Richard et al. (2005) we note that the “high” Li abundances of the hottest stars in the sample (among which is the primary of CS 22876–032), preclude any clear resemblance between the two pictures. Therefore, current pure diffusion models seem unable to explain at the same time the behaviour of Li abundances with [Fe/H] and  $T_{\text{eff}}$ . It is possible, however, that they may do so, after an *ad hoc* parametrisation of turbulence with metallicity.

Recently Korn et al. (2006, 2007) have found that the models of Richard et al. (2005), with a suitable value for the turbulent diffusion coefficient, can explain the 0.12 dex difference in A(Li) they find between stars at the turn-off and on the sub-giant branch stars of the globular cluster NGC 6397. The same authors, however point out that assigning temperatures for the TO stars, hotter by 170 K (therefore close to the temperatures adopted by Bonifacio et al. 2002 for the TO stars of this cluster), such a difference would vanish.

Though suggestive, the applicability of such turbulent diffusive models remains to be proven. The main cause of concern is the parametrisation of the turbulent diffusive coefficient, which is linked to a fixed temperature, and not to the bottom of the convective zone (Richard et al. 2002).

In order to strengthen the observational constraints on such models and refine the estimates of the scatter and slope (or lack thereof) of the extreme metal-poor end of the *Spite Plateau*, further high-quality spectroscopy of EMP stars and additional accurate constraints on the effective temperatures of the whole sample are highly desirable.

## 6.2. Oxygen

Fig. 14 compares our 3D-LTE O abundances obtained from OH UV bands in CS 22876–032 with the high-quality measurements of Paper V for giant stars (mixed and unmixed), obtained from the [OI] 630nm line. We note that we have computed the 3D-LTE [O/Fe] ratios using the true 3D-LTE oxygen abundances

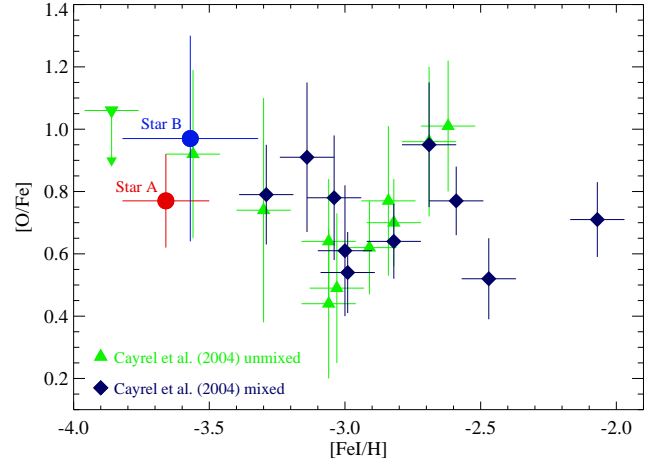


**Fig. 14.** 3D [O/Fe] ratios of the stars in CS 22876–032 (circles) and in the metal-poor giants of Paper V. Triangles: “unmixed”, rhombs “mixed” stars; downward triangle with arrow: upper limit for CS 22172–002).

and the (3D) Fe I abundances. We have chosen Fe I rather than Fe II abundances as the reference, because their sensitivity to the surface gravity is similar as that of the OH bands. The reader might wonder why we find different O abundances for stars A and B, but they are in fact consistent within the error bars, which mainly reflect the uncertainties in the effective temperature (see Table 4).

The abundances derived from [OI] are the raw values obtained from 1D-LTE model atmospheres. One worry is the possible effects of granulation on the abundances derived from the [OI] line in giants. In a recent paper, Collet et al. (2007) investigated the 3D effects in giant stars and found very small corrections for the [OI] lines for metallicities down to  $-2.0$ , but sizeable (almost 0.2 dex) downward corrections for [O/Fe] at metallicity  $-3.0$  (their Fig. 13 and Table 3). If we apply the corrections interpolated and extrapolated from Table 3 of Collet et al. (2007) to the giants of Paper V, the [O/Fe] decreases in all the giants and the good agreement between CS 22876–032 and the giants no longer holds. The mean [O/Fe] of the giants would be 0.51, while that of CS 22876–032 is 0.87. If instead we take the measurements of Paper V at face value, the mean [O/Fe] is 0.72.

At present we have no full 3D models for giant stars, however, from a few snapshots for models of  $T_{\text{eff}} = 4900$ ,  $\log g = 2.0$  and metallicity  $-2.0$  and  $-3.0$  we find little difference at the two metallicities, and very small 3D corrections. The 3D – 1D<sub>LHD</sub> abundance correction amounts to  $-0.006$  dex at metallicity  $-2.0$  and  $-0.037$  dex at  $-3.0$ , which is negligible. For our CO<sup>5</sup>BOLD models of giants the difference between the mean 3D temperature structure and a corresponding 1D<sub>LHD</sub> ( $\alpha_{\text{MLT}} = 1.0$ ) model is not large. In particular we do not find the substantial cooling of the highest photospheric layers at metallicity  $-3.0$ , which Collet et al. (2007) find (see their Fig. 1). Moreover, the mean 3D temperature profile is slightly hotter than the 1D<sub>LHD</sub> temperature profile in the [OI] 630 nm line-forming layers around  $\log \tau \sim -1$ . The differences between our assessment of the impact of granulation on the abundances derived from the [OI] 630 nm line in giants, and that of Collet et al. (2007), will be further investigated in the future. This might be rooted in the different binning schemes adopted by the two codes for the opacity (4 opacity bins for the Stein & Nordlund code and 6 opacity bins for CO<sup>5</sup>BOLD). In any case we believe that, at present, it is safer

not to apply any 3D correction to the O abundances derived for giants from the [OI] 630 nm line.

In Paper V we found that the mean value of [O/Fe] in the range  $-3.6 < [\text{Fe}/\text{H}] < -2.5$  was about  $0.72 \pm 0.17$ . The weighted average value in CS22876–032, [O/Fe] =  $0.83 \pm 0.15$ , agrees with this determination. This mean value does not exclude a slight increase of the ratio [O/Fe] in the range  $-3.6 < [\text{Fe}/\text{H}] < -2.5$  as seen in the theoretical predictions of the chemical evolution models presented by François et al. (2004). A more detailed discussion of the general behaviour of oxygen with metallicity will be treated in forthcoming investigations, hopefully after 3D corrections will be determined for all the stars, and for different lines of oxygen, Fe I and Fe II.

### 6.3. The Odd-Z light elements

The LTE [Na/Fe] abundance ratios of both stars appear consistent with the Galactic trend of this element in EMP giants (Cayrel et al. 2004), subgiants and turn-off stars of similar metallicity (Andrievsky et al. 2007). NLTE corrections are expected to be larger for the metal-poor giants than for dwarfs. We have estimated the NLTE corrections<sup>6</sup> for Na to be  $\Delta_{\text{NLTE}} \lesssim -0.06$  dex, according to the NLTE corrections reported in Table 2 of Andrievsky et al. (2007). After applying these corrections, Na abundances of the CS 22876–032 dwarfs remain compatible with those of metal-poor giants and dwarfs, which exhibit almost a constant ratio [Na/Fe]  $\sim -0.20$  in the metallicity range  $-4.0 < [\text{Fe}/\text{H}] < -2.5$ .

The LTE [Al/Fe] abundance ratios of the dwarfs in this system are  $\sim 0.5$  dex larger than those in metal-poor giants with similar iron content. However, aluminium is also expected to exhibit significant NLTE corrections (Baumüller & Gehren 1997), which might explain this difference, as was the case for Na. This element also exhibits an almost constant ratio [Al/Fe]  $\sim -0.10$  for giants in the metallicity range  $-4.0 < [\text{Fe}/\text{H}] < -2.5$  when a fixed NLTE correction of  $+0.65$  dex is considered.

Within the errors, [Sc/Fe] is consistent with, although 0.2–0.3 dex lower than, the [Sc/Fe] ratio in EMP giants which shows an almost constant ratio [Sc/Fe]  $\sim 0$ . Note that the [X/Fe] ratios given in Table 3 were computed relative to Fe II for ionised species. As noted in § 5.2.3, the Fe II abundances are less reliable than those for Fe I because the Fe II lines in EMP dwarfs are very weak, especially for star B in CS 22876–032. Therefore, [X/Fe] for ionised species in star B should be regarded with caution.

### 6.4. The $\alpha$ elements

The [Mg/Fe] ratios in both stars of CS 22876–032 seems to be fairly consistent with those found in EMP giants (Cayrel et al. 2004), subgiants and dwarfs (Cohen et al. (2004), Bonifacio et al. 2007, in prep.), at the level of  $\sim 0.3 - 0.4$  dex.

[Ca/Fe] was derived from both Ca I and Ca II lines, which yield similar [Ca/H] abundances, at least for the primary star. However, although the [Ca/Fe] ratios differ by  $\sim 0.2$  dex, they seem to be slightly lower than those measured in metal-poor giants and dwarfs, where a constant [Ca/Fe]  $\sim 0.4$  is seen.

[Si/Fe] also seems to be low, at [Si/Fe]  $\sim -0.1$  for stars A and  $\sim +0.1$  for the secondary, compared to the constant [Si/Fe]  $\sim 0.4$  for metal-poor giants. However, other metal-poor dwarfs show similar abundances, which might be related to the different Si lines used in giants and dwarfs (Bonifacio et al. 2007, in prep.).

Finally, [Ti/Fe] is constant at  $\sim 0.3$  in EMP giants. While we find a similar result for star A, [Ti/Fe] in star B is completely different due to its high Fe II abundance. We note that the standard deviation in [Ti/Fe] is relatively high in both stars ( $\sigma \sim 0.3$ ), although the mean abundances are better determined when averaging the results from the 19 lines in star A and 12 in B.

### 6.5. The iron-peak elements

Chromium was derived from both Cr I and Cr II lines, and we find a difference of  $\sim 0.2$  dex for the [Cr/Fe] ratios. [Cr I/Fe I] in CS 22876–032 appears to agree with that in other EMP dwarfs, but is slightly higher than seen in EMP giants.

The ratio [Mn/Fe] is consistent with the other EMP giants and dwarfs, at [Mn/Fe]  $\sim -0.5$ . [Ni/Fe] also agrees with the values reported for EMP giants, which show a constant [Ni/Fe]  $\sim 0$ .

Cobalt is found to be slightly enhanced in CS 22876–032 relative to the gradually increasing trend of [Co/Fe] with decreasing [Fe/H] observed in giants, although marginally compatible within the errors.

### 6.6. Could CS 22876–032 be a triple system ?

One might ask whether a third star in CS 22876–032 might contribute significantly to the total light and the veiling of the lines of the two main components we have discussed so far. Such a star would need to have a mass above  $\sim 0.5 M_{\odot}$  in order to have any significant effect on the observed spectrum. The presence of such a third star can be ruled out by two independent pieces of evidence.

First, we have individual spectra of CS 22876–032 with S/N ratios  $\sim 100$  in the region of the Mg I b triplet. These are among the strongest stellar lines seen in these EMP stars and would be at least as strong in the third star. The Cayrel formula predicts that any line with an EW above  $\sim 0.15$  pm would be detected at the  $3\sigma$  level. Assuming  $\text{teff} = 5500\text{K}$  and  $\log g = 4.7$  (from the isochrone) plus [Fe/H] =  $-3.6$  and [Mg/Fe] =  $+0.2$  for the hypothetical third star, we need to dilute the strongest line of the Mg I b triplet at 518.36 nm which would show an intrinsic EW of  $\sim 15.0$  pm. In Appendix A we define the veiling factors for a triple system and conclude that the non-detection of the 518.36 nm line requires  $f_3 > 100$ . We can therefore conclude that any third star contributes negligibly to the total light of CS 22876–032.

A second line of evidence is available from the radial velocities, which are accurate to  $\sim 1 \text{ km s}^{-1}$  and cover a period of 16 years. Any third star of mass comparable to A and B should leave significant trends in the velocity residuals from the orbital solution for periods shorter than several decades. We have therefore attempted sinusoidal fits to the velocity residuals for both stars and find periods of the order of 1300 days in both cases. First, the standard deviations around these fits are 0.83 and 0.51  $\text{km s}^{-1}$ , well below the purely observational errors, which shows that these results cannot be statistically significant. Second, a period ratio of  $\sim 3$  between the outer and inner orbits is far too small for a triple system to be dynamically stable. A white dwarf in an orbit of much longer period is a possibility, but would not be detectable in our spectra.

In summary, we conclude that the abundance results reported here cannot be significantly affected by light from a third star in the system – certainly not the discrepant Li abundances of the two stars.

<sup>6</sup>  $\Delta_{\text{NLTE}} = \log \epsilon(\text{X})_{\text{NLTE}} - \log \epsilon(\text{X})_{\text{LTE}}$



## 7. Summary

Our high-resolution VLT/UVES observations of the double-lined spectroscopic binary CS 22876–032 confirm that it harbours the most metal-poor dwarfs known so far. Our improved orbital elements, together with published photometry and theoretical isochrones, enable us to determine stellar parameters of  $T_{\text{eff},A} = 6500 \pm 100$  K and  $\log g_A = 4.4 \pm 0.1$  for the primary (star A) and  $T_{\text{eff},B} = 5900 \pm 150$  K and  $\log g_B = 4.6 \pm 0.1$  for the secondary (star B).

Using 1D OSMARCS models and the TURBOSPECTRUM code, we determine abundances of Li, O, Na, Mg, Al, Si, Ca, Sc, Ti, Cr, Mn, Fe, Co, and Ni, correcting the observed spectra for the veiling from the continuum flux of the other star. We find  $[\text{Fe}/\text{H}] = -3.66 \pm 0.16$  and  $[\text{Fe}/\text{H}] = -3.57 \pm 0.25$  for star A and B, respectively. Using CO<sup>5</sup>BOLD model atmospheres to estimate 3D abundance corrections, we compute full 3D spectrum synthesis using the Linfor3D code for Li and O to estimate the 3D – 1D<sub>LHD</sub> corrections, while we use a horizontal and temporal average of the 3D model to compute  $\langle 3D \rangle$  abundances with TURBOSPECTRUM for the rest of elements. In general, we find ( $\langle 3D \rangle$  – 1D<sub>MARCS</sub>) corrections to be  $\lesssim 0.1$  dex, negative for neutral species and positive for ionised species; for Fe in particular, we find corrections to be  $\sim -0.12$  (A) and  $\sim -0.07$  (B).

The  $[\alpha/\text{Fe}]$  ratios are consistent with our earlier results for EMP giants (Cayrel et al. 2004, First Stars V), although Ca and Si are slightly low ( $[\text{X}/\text{Fe}] \lesssim 0$ ), but actually consistent with our results for other EMP dwarfs (Bonifacio et al. 2007, in prep.).  $[\text{Na}/\text{Fe}]$  appears consistent with both EMP giants and dwarfs when NLTE corrections are considered. The LTE value of  $[\text{Al}/\text{Fe}]$  is not consistent with those in EMP giants, but Al is severely affected by NLTE effects, which may solve this discrepancy. The iron-peak elements follow the established trends in EMP giants and dwarfs.

Our high-quality spectra allowed us to measure the Li doublet in both stars of CS 22876–032 for the first time. We find NLTE Li abundances of  $2.18 \pm 0.05$  and  $1.77 \pm 0.09$  for stars A and B, respectively. While the Li abundance of star A corresponds to the level of the Spite plateau, the secondary star has a significantly lower abundance. This discrepancy may be resolved by assuming that the secondary star has been subject to significant Li depletion, which, according to standard Li depletion isochrones, would have been the case if the star were 350K cooler than assumed by our analysis. Full 3D corrections for Li are estimated to be  $\sim -0.3$  (A) and  $\sim -0.2$  (B); however, these computations were performed in LTE, and 3D NLTE corrections are needed to confirm the sign and value of these corrections.

The near-UV part of our VLT/UVES spectra enabled us to measure oxygen abundances from the OH bands. We find 1D  $[\text{O}/\text{Fe}]$  values of  $2.14 \pm 0.15$  (A) and  $1.81 \pm 0.33$  (B) and compute full 3D corrections for the OH lines, which turn out to be  $-1.5$  (A) and  $-1.0$  dex (B). Using these corrections and the  $\langle 3D \rangle$  Fe I abundances, we determine 3D  $[\text{O}/\text{Fe}]$  ratios of  $0.77 \pm 0.15$  (A) and  $0.97 \pm 0.33$  (B). These 3D  $[\text{O}/\text{Fe}]$  ratios are consistent with those derived from the  $[\text{OI}]$  line in EMP giants of similar metallicity, where 3D corrections should not be significant.

**Acknowledgements.** We are grateful to A. Chieffi and M. Limongi, for computing, at our request, isochrones appropriate for the metallicity of CS 22876–032 and for many interesting discussions on the evolution of extremely low metallicity dwarfs. J. I., P. B. and H.-G. L. acknowledge support from the EU contract MEXT-CT-2004-014265 (CIFIST). PB also acknowledges support from MIUR - PRIN grant 2004025729. BN and JA thank the Carlsberg Foundation and the Danish Natural Science Research Council for support for this work. TCB and TS acknowledge partial support from the US National Science Foundation under grants AST 04-06784, AST 07-07776, as well as from grant PHY

02-15783; Physics Frontier Center / Joint Institute for Nuclear Astrophysics (JINA). BN and JA acknowledge support from the Carlsberg Foundation and the Danish Natural Science Research Council. This publication makes use of data products from the Two Micron All Sky Survey, which is a joint project of the University of Massachusetts and the Infrared Processing and Analysis Center/California Institute of Technology, funded by the National Aeronautics and Space Administration and the National Science Foundation. This work has also made use of the IRAF facilities and the SIMBAD database, operated at CDS, Strasbourg, France.

## References

- Alvarez R., Plez B., 1998, A&A, 330, 1109  
 Andrievsky, S. M., Spite, M., Korotin, S. A., Å. 2007, A&A, 464, 1081  
 Asplund, M., & García Pérez, A. E. 2001, A&A, 372, 601  
 Asplund, M., Gustafsson, B., Kiselman, D., Eriksson, K. 1997, A&A, 318, 521  
 Asplund, M., Nordlund, Å., Trampedach, R., Stein, R.F. 1999, A&A, 346, L17  
 Asplund, M., Carlsson, M., & Botnen, A. V. 2003, A&A, 399, L31  
 Asplund, M., Lambert, D. L., Nissen, P. E., Primas, F., & Smith, V. V. 2006, ApJ, 644, 229  
 Baumüller, D., & Gehren, T. 1997, A&A, 325, 1088  
 Barklem, P. S., Piskunov, N., & O'Mara, B. J. 2000, A&A, 363, 1091  
 Barklem, P. S., Stempels, H. C., Allende Prieto, C., Kochukhov, O. P., Piskunov, N., & O'Mara, B. J. 2002, A&A, 385, 951  
 Beers, T. C., Preston, G. W., & Shectman, S. A. 1985, AJ, 90, 2089  
 Bessell, M. S., & Norris, J. 1984, ApJ, 285, 622  
 Bessell, M. S., & Brett, J. M. 1988, PASP, 100, 1134  
 Bessell, M. S., Sutherland, R. S., & Ruan, K. 1991, ApJ, 383, L71  
 Bessell, M. S., Castelli, F. & Plez, B. 1998, A&A, 333, 231  
 Boesgaard, A. M., Deliyannis, C. P., King, J. R., Ryan, S. G., Vogt, S. S., & Beers, T. C. 1999, AJ, 117, 1549  
 Boesgaard, A. M., King, J. R., Deliyannis, C. P., & Vogt, S. S. 1999, AJ, 117, 492  
 Boesgaard, A. M., & Novicki, M. C. 2006, ApJ, 641, 1122  
 Bonifacio, P., Castelli, F., Molaro, P. 1990, in proceedings of “Chemical and Dynamical Evolution of Galaxies”, ed. F. Ferrini, J. Franco, F. Matteucci, p. 67 ETS Editrice, Pisa  
 Bonifacio, P. & Molaro, P. 1997, MNRAS, 285, 847  
 Bonifacio, P., et al. 2002, A&A, 390, 91  
 Bonifacio, P., Molaro, P., Sivarani, T. Å. 2007, A&A, 462, 851 (Paper VII)  
 Caffau, E., Faraggiana, R., Bonifacio, P., Ludwig, H.-G., & Steffen, M. 2007, A&A, 470, 699  
 Caffau E., Ludwig, H.-G., Steffen, M., Ayres, T.R., Cayrel, R., Bonifacio, P., B. Freytag, B. Plez A&Ain preparation  
 Carlsson, M., Rutten, R. J., Bruls, J. H. M. J., & Shchukina, N. G. 1994, A&A, 288, 860  
 Carpenter, J. M. 2001, AJ, 121, 2851  
 Castelli, F., & Hubrig, S. 2004, A&A, 425, 263  
 Castelli, F. & Kurucz, R. L. 2003, in IAU Symposium, ed. N. Piskunov, W. W. Weiss, & D. F. Gray, 20P  
 Cayrel, R. 1988, IAU Symp. 132: The Impact of Very High S/N Spectroscopy on Stellar Physics, 132, 345  
 Cayrel, R., & Steffen, M. 2000, The Light Elements and their Evolution, 198, 437  
 Cayrel, R., Depagne, E., Spite, M. Å. 2004, A&A, 416, 1117 (Paper V)  
 Cayrel, R., Steffen, M., Chand, H. Å. 2007, A&A, 473, L37  
 Charbonneau, P. 1995, ApJS, 101, 309  
 Charbonnel, C., & Primas, F. 2005, A&A, 442, 961  
 Cohen, J. G., Christlieb, N., McWilliam, A., Å. 2004, ApJ, 612, 1107  
 Collet, R., Asplund, M., & Trampedach, R. 2007, A&A, 469, 687  
 Deliyannis, C. P., Demarque, P., & Kawaler, S. D. 1990, ApJS, 73, 21  
 Edvardsson, B., Andersen, J., Gustafsson, B., Lambert, D.L., Nissen, P.E., Tomkin, J. 1993, A&A, 275, 101  
 François, P., Depagne, E., Hill, V., Å. 2003, A&A, 403, 1105 (Paper III)  
 François, P., Matteucci, F., Cayrel, R., Spite, M., Spite, F., & Chiappini, C. 2004, A&A, 421, 613  
 Frebel, A., et al. 2005, Nature, 434, 871  
 Freytag, B., Steffen, M., & Dorch, B. 2002, Astronomische Nachrichten, 323, 213  
 Fuhrmann, K., Axer, M., & Gehren, T. 1993, A&A, 271, 451  
 Gangrsky, Y., et al. 2006, Hyperfine Interactions, 171, 209  
 Gilmore, G., Gustafsson, B., Edvardsson, B., & Nissen, P. E. 1992, Nature, 357, 379  
 Goldberg, D., Mazeh, T., Latham, D. W., Å. 2002, AJ, 124, 1132  
 Grainge, K., Carreira, P., Cleary, K., Å. 2003, MNRAS, 341, L23  
 Grevesse, N., & Sauval, A. 2000, Encyclopedia of Astronomy and Astrophysics, Edited by Paul Murdin, article 1979. Bristol: Institute of Physics Publishing

Gustafsson, B., Bell, R.A., Eriksson, K., Nordlund Å., 1975, *A&A*, 42, 407  
 Gustafsson B., Edvardsson B., Eriksson K., Graae-Jørgensen U., Mizuno-Wiedner, M., Plez, B., 2003, in *Stellar Atmosphere Modeling*, eds. I. Hubeny, D. Mihalas, K. Werner, ASP Conf. Series 288, 331.  
 Harrington, R. S. 1977, *Revista Mexicana de Astronomía y Astrofísica*, vol. 3, 3, 139  
 Israelian, G., García López, R. J., & Rebolo, R. 1998, *ApJ*, 507, 805  
 Israelian, G., Rebolo, R., García López, R. J., Bonifacio, P., Molaro, P., Basri, G., & Shchukina, N. 2001, *ApJ*, 551, 833  
 Khodykin, S. A., Zakharov, A. I., & Andersen, W. L. 2004, *ApJ*, 615, 506  
 Korn, A. J., Grundahl, F., Richard, O., Barklem, P. S., Mashonkina, L., Collet, R., Piskunov, N., & Gustafsson, B. 2006, *Nature*, 442, 657  
 Korn, A. J., Grundahl, F., Richard, O., Barklem, P. S., Mashonkina, L., Collet, R., Gustafsson, B., & Piskunov, N. 2007, *ApJ*, in press, arXiv:0709.0639  
 Kurucz, R. 1993a, *ATLAS9 Stellar Atmosphere Programs and 2 km/s grid*. Kurucz CD-ROM No. 13. Cambridge, Mass.: Smithsonian Astrophysical Observatory, 1993., 13  
 Kurucz, R. L. 2005a, *Memorie della Società Astronomica Italiana Supplement*, 8, 14  
 Kuo, C. L., Ade, P. A. R., Bock, J. J., Å. 2004, *ApJ*, 600, 32  
 Latham, D. W., Stefanik, R. P., Torres, G., Å. 2002, *AJ*, 124, 1144  
 Lomb, N. R. 1976, *Ap&SS*, 39, 447  
 Ludwig, H.-G., & Steffen, M. 2007, to appear in the *Proceedings of the ESO/Lisbon/Aveiro Workshop "Precision Spectroscopy in Astrophysics"*, eds. L. Pasquini, M. Romaniello, N.C. Santos, and A. Correia, arXiv:0704.1176  
 McWilliam, A., Preston, G. W., Sneden, C., & Searle, L. 1995, *AJ*, 109, 2757  
 Meléndez, J., & Ramírez, I. 2004, *ApJ*, 615, L33  
 Molaro, P., & Castelli, F. 1990, *A&A*, 228, 426  
 Molaro, P., Bonifacio, P., Castelli, F., & Pasquini, L. 1997, *A&A*, 319, 593  
 Nissen, P. E. 1989, *The Messenger*, 58, 40  
 Nissen, P. E., Primas, F., Asplund, M., & Lambert, D. L. 2002, *A&A*, 390, 235  
 Norris, J. E., Peterson, R. C., Beers, T. C. 1993, *ApJ*, 415, 797  
 Norris, J. E., Beers, T. C. & Ryan, S. G. 2000, *ApJ*, 540, 456  
 Pearson, T. J., Mason, B. S., Readhead, A. C. S., Å. 2003, *ApJ*, 591, 556  
 Pickering, J. C. 1996, *ApJS*, 107, 811  
 Plez, B., Brett, J.M., Nordlund, Å. 1992, *A&A*, 256, 551  
 Preston, G. W., Shectman, S. A., Beers, T. C. 1991, *ApJS*, 76, 1001  
 Primas, F. 2002, *Ap&SS*, 281, 195  
 Richard, O., Michaud, G., Richer, J., Turcotte, S., Turck-Chièze, S., & VandenBerg, D. A. 2002, *ApJ*, 568, 979  
 Richard, O., Michaud, G., Richer, J. 2005, *ApJ*, 619, 538  
 Rebolo, R., Battye, R. A., Carreira, P., et al. Å. 2004, *MNRAS*, 353, 747  
 Ryan, S. G., Norris, J. E., Bessell, M. S., & Deliyannis, C. 1992, *ApJ*, 388, 184  
 Ryan, S. G., Norris, J. E., & Beers, T. C. 1999, *ApJ*, 523, 654  
 Sbordone, L. 2005, *Memorie della Società Astronomica Italiana Supplement*, 8, 61  
 Sbordone, L., Bonifacio, P., Castelli, F., & Kurucz, R. L. 2004, *Memorie della Società Astronomica Italiana Supplement*, 5, 93  
 Scargle, J. D. 1982, *ApJ*, 263, 835  
 Schuster, W. J., Parrao, L., & Contreras Martinez, M. E. 1993, *A&AS*, 97, 951  
 Schuster, W. J., Nissen, P. E., Parrao, L., Beers, T. C., & Overgaard, L. P. 1996, *A&AS*, 117, 317  
 Shchukina, N. G., Trujillo Bueno, J., & Asplund, M. 2005, *ApJ*, 618, 939  
 Slettebak, A., & Brundage, R. K. 1971, *AJ*, 76, 338  
 Spergel, D. N., Bean, R., Doré, O., Å. 2003, *ApJS*, 148, 175  
 Spergel, D. N., Verde, L., Peiris, H. V., Å. 2007, *ApJS*, 170, 377  
 Spite, M. & Spite, F. 1982, *Nature*, 297, 483  
 Spite, F., & Spite, M. 1982, *A&A*, 115, 357  
 van't Veer-Menneret, C., & Mégessier, C. 1996, *A&A*, 309, 879  
 Wahlgren, G. M. 2005, *Memorie della Società Astronomica Italiana Supplement*, 8, 108  
 Wedemeyer, S., Freytag, B., Steffen, M., Ludwig, H.-G., & Holweger, H. 2003, *Astronomische Nachrichten*, 324, 410  
 Wichmann, R., Schmitt, J. H. M. M., & Hubrig, S. 2003, *A&A*, 400, 293

## Appendix A: Veiling factors for a triple system.

In this appendix we derive the expression for the veiling factors of a triple system. In fact they are a trivial extension of those for a double system, however since they are not readily found in any paper or book we know of, we provide them here for the reader's convenience.

We shall use the following notation:

$\lambda$	wavelength
$s_i(i = 1, 2, 3)$	the flux spectrum $s_\lambda$ of the $i_{th}$ component
$c_i(i = 1, 2, 3)$	the continuum flux spectrum $c_\lambda$ of the $i_{th}$ component
$d_i(i = 1, 2, 4)$	the line depression = $c_i - s_i$
$EW_i(i = 1, 2, 3)$	the intrinsic equivalent width of a spectral line of the $i_{th}$ component
$EW_i^{obs}(i = 1, 2, 3)$	the observed equivalent width of a spectral line of the $i_{th}$ component
$EW_{123}^{obs}$	the observed equivalent width of the three components.

In any orbital phase we have:

$$EW_{123}^{obs} = \int_{\lambda 1}^{\lambda 2} \frac{d_1 + d_2 + d_3}{c_1 + c_2 + c_3} d\lambda$$

Where the interval  $[\lambda 1, \lambda 2]$  includes the desired spectral feature, which we assume to be isolated. Considering that the continuum fluxes can be assumed to be constant over the integration interval this can be re-written as:

$$EW_{123}^{obs} = \frac{c_1}{c_1+c_2+c_3} \int_{\lambda 1}^{\lambda 2} \frac{d_1}{c_1} d\lambda + \frac{c_2}{c_1+c_2+c_3} \int_{\lambda 1}^{\lambda 2} \frac{d_2}{c_2} d\lambda + \frac{c_3}{c_1+c_2+c_3} \int_{\lambda 1}^{\lambda 2} \frac{d_3}{c_3} d\lambda$$

We now define the veiling factors as  $f_i = (c_1 + c_2 + c_3)/c_i$  and consider a phase in which the radial velocities are such that the line of each component is isolated and not blended with the others, then one has:

$$EW_{123}^{obs} = EW_1^{obs} + EW_2^{obs} + EW_3^{obs}$$

and noting that :

$$\int_{\lambda 1}^{\lambda 2} \frac{d_i}{c_i} d\lambda = EW_i$$

one has that :

$$EW_1^{obs} + EW_2^{obs} + EW_3^{obs} = EW_1/f_1 + EW_2/f_2 + EW_3/f_3$$

finally considering that in this phase the lines are not overlapping this equality implies:

$$EW_i = f_i EW_i^{obs}$$

# Online Material



**Table A.1.** Line data, equivalent widths, veiling factors and 1D abundances of CS 22876-032A,B

Specie	$\lambda$ (nm)	$\chi$ (eV)	$\log gf$	$EW_{A,obs}$ (pm)	$f_{A,1D}$	$A(X)_{A,1D}$ (dex)	$EW_{B,obs}$ (pm)	$f_{B,1D}$	$A(X)_{B,1D}$ (dex)
Na I	588.9951	0.000	0.112	1.40	1.35	2.63	–	–	–
Na I	589.5924	0.000	-0.191	0.79	1.35	2.64	0.49	3.87	2.54
Mg I	333.6674	2.720	-1.230	1.07	1.32	4.57	0.90	4.16	4.68
Mg I	382.9355	2.710	-0.207	5.01	1.31	4.41	2.06	4.24	4.29
Mg I	383.2304	2.710	0.146	6.03	1.31	4.29	2.87	4.25	4.35
Mg I	383.8290	2.720	0.415	6.89	1.30	4.21	2.77	4.31	4.06
Mg I	416.7271	4.340	-1.000	0.23	1.29	4.84	0.11	4.41	4.86
Mg I	517.2684	2.710	-0.380	4.88	1.33	4.47	2.42	4.04	4.41
Mg I	518.3604	2.720	-0.158	5.73	1.33	4.43	3.24	4.03	4.52
Mg I	552.8405	4.340	-0.341	0.60	1.34	4.58	0.16	3.94	4.25
Mg I	880.6756	4.340	-0.137	0.81	1.39	4.41	0.62	3.57	4.50
Al I	394.4006	0.000	-0.623	1.51	1.28	2.74	1.12	4.54	2.88
Al I	396.1520	0.010	-0.323	1.41	1.31	2.42	1.16	4.24	2.56
Si I	390.5523	1.910	-1.090	1.55	1.29	3.80	1.32	4.42	4.07
Ca I	422.6728	0.000	0.240	3.60	1.30	2.71	1.70	4.39	2.68
Ca II	317.9331	3.150	0.512	4.08	1.30	2.62	1.36	4.28	2.57
Ca II	370.6024	3.120	-0.480	1.41	1.34	2.58	–	–	–
Ca II	373.6902	3.150	-0.173	3.22	1.33	2.84	0.68	4.04	2.53
Sc II	361.3829	0.020	0.416	0.42	1.33	-0.69	0.42	4.01	-0.40
Sc II	424.6822	0.310	0.240	0.37	1.30	-0.44	0.16	4.38	-0.41
Ti II	316.8532	0.150	-0.310	2.35	1.30	1.66	0.70	4.29	1.34
Ti II	323.4520	0.050	0.426	4.55	1.31	1.54	1.64	4.25	1.34
Ti II	323.6578	0.030	0.234	4.11	1.31	1.56	1.72	4.25	1.59
Ti II	324.1994	0.000	-0.045	3.20	1.31	1.51	1.75	4.24	1.86
Ti II	325.1918	0.010	-0.579	1.54	1.31	1.52	0.65	4.23	1.39
Ti II	332.2941	0.150	-0.093	2.38	1.32	1.44	1.23	4.17	1.53
Ti II	332.9453	0.140	-0.274	2.53	1.32	1.65	1.33	4.17	1.78
Ti II	338.0279	0.050	-0.570	3.38	1.32	2.12	1.33	4.14	1.98
Ti II	338.7846	0.030	-0.432	2.29	1.32	1.63	1.01	4.14	1.54
Ti II	344.4314	0.150	-0.810	1.02	1.32	1.63	–	–	–
Ti II	345.6388	2.060	-0.230	0.41	1.32	2.32	–	–	–
Ti II	347.7187	0.120	-0.967	1.17	1.32	1.83	0.58	4.08	1.76
Ti II	348.9741	0.140	-1.920	0.40	1.33	2.27	–	–	–
Ti II	350.0340	0.120	-2.020	0.37	1.33	2.32	–	–	–
Ti II	375.9296	0.610	0.270	2.39	1.32	1.33	0.94	4.16	1.26
Ti II	376.1323	0.570	0.170	2.36	1.32	1.39	1.07	4.16	1.43
Ti II	391.3468	1.120	-0.410	0.39	1.28	1.48	–	–	–
Ti II	402.8343	1.890	-0.990	0.15	1.29	2.30	–	–	–
Ti II	518.8680	1.580	-1.050	0.14	1.33	2.01	–	–	–
Cr I	357.8684	0.000	0.409	0.85	1.33	1.79	0.61	4.03	1.61
Cr I	425.4332	0.000	-0.110	0.45	1.30	1.83	0.28	4.37	1.63
Cr I	427.4796	0.000	-0.230	0.32	1.30	1.79	0.16	4.36	1.48
Cr I	428.9716	0.000	-0.360	0.46	1.30	2.09	0.58	4.35	2.27
Cr I	520.6038	0.940	0.020	0.13	1.33	1.92	–	–	–
Cr II	313.2053	2.480	0.451	2.85	1.30	2.29	1.10	4.32	2.37
Mn II	344.1988	1.780	-0.270	0.54	1.32	1.38	0.32	4.11	1.53

**Table A.1.** Continued.

Specie	$\lambda$ (nm)	$\chi$ (eV)	$\log gf$	$EW_{A,obs}$ (pm)	$f_{A,1D}$	$A(X)_{A,1D}$ (dex)	$EW_{B,obs}$ (pm)	$f_{B,1D}$	$A(X)_{B,1D}$ (dex)
Fe I	347.5450	0.090	-1.054	3.24	1.32	3.99	1.89	4.09	4.07
Fe I	347.6702	0.120	-1.507	1.96	1.32	4.05	1.40	4.08	4.07
Fe I	349.0574	0.050	-1.105	2.91	1.33	3.90	1.93	4.07	4.11
Fe I	356.5379	0.960	-0.133	2.96	1.33	3.75	1.90	4.04	3.92
Fe I	358.1193	0.860	0.406	4.17	1.33	3.55	2.81	4.03	3.89
Fe I	360.8859	1.010	-0.100	3.39	1.33	3.91	2.17	4.01	4.13
Fe I	361.8768	0.990	-0.003	3.55	1.33	3.85	2.25	4.00	4.06
Fe I	364.7843	0.920	-0.194	3.29	1.33	3.72	2.24	4.00	4.09
Fe I	381.5840	1.490	0.237	3.79	1.30	3.88	1.61	4.34	3.77
Fe I	382.0425	0.860	0.119	5.15	1.30	3.89	2.00	4.30	3.63
Fe I	382.5881	0.920	-0.037	4.10	1.31	3.76	2.00	4.26	3.82
Fe I	382.7823	1.560	0.062	2.57	1.31	3.79	1.29	4.25	3.71
Fe I	384.0438	0.990	-0.506	2.26	1.30	3.76	1.11	4.34	3.60
Fe I	384.1048	1.610	-0.045	2.05	1.30	3.78	0.88	4.35	3.54
Fe I	384.9967	1.010	-0.871	1.26	1.29	3.79	1.09	4.46	3.99
Fe I	385.6372	0.050	-1.286	3.23	1.28	3.96	1.76	4.52	4.16
Fe I	385.9911	0.000	-0.710	5.44	1.28	4.03	2.42	4.54	4.08
Fe I	386.5523	1.010	-0.982	1.03	1.28	3.79	–	–	–
Fe I	387.2501	0.990	-0.928	1.58	1.29	3.95	0.99	4.49	3.94
Fe I	387.8018	0.960	-0.914	1.59	1.30	3.91	1.29	4.36	4.13
Fe I	388.6282	0.050	-1.076	2.64	1.32	3.60	2.18	4.17	4.17
Fe I	388.7048	0.920	-1.144	1.02	1.32	3.87	1.15	4.16	4.15
Fe I	389.5656	0.110	-1.670	1.59	1.31	3.92	1.43	4.19	4.15
Fe I	389.9707	0.090	-1.531	2.16	1.31	3.94	1.66	4.28	4.23
Fe I	390.2946	1.560	-0.466	1.10	1.30	3.79	0.91	4.35	3.93
Fe I	390.6480	0.110	-2.243	0.77	1.29	4.09	0.63	4.44	4.05
Fe I	392.0258	0.120	-1.746	1.39	1.28	3.91	1.28	4.58	4.20
Fe I	392.7920	0.110	-1.522	2.26	1.28	3.97	1.44	4.58	4.12
Fe I	404.5812	1.490	0.280	3.96	1.29	3.85	1.38	4.47	3.52
Fe I	406.3594	1.560	0.062	2.88	1.29	3.84	1.49	4.47	3.90
Fe I	407.1738	1.610	-0.022	2.54	1.29	3.87	1.26	4.44	3.83
Fe I	413.2058	1.610	-0.675	0.98	1.29	3.96	0.67	4.42	3.96
Fe I	414.3868	1.560	-0.511	1.24	1.29	3.87	1.07	4.43	4.09
Fe I	420.2029	1.490	-0.708	0.93	1.29	3.85	0.70	4.40	3.89
Fe I	425.0787	1.560	-0.714	0.58	1.30	3.69	0.49	4.37	3.74
Fe I	426.0474	2.400	0.109	0.72	1.30	3.71	0.28	4.37	3.43
Fe I	427.1761	1.490	-0.164	2.43	1.30	3.86	1.23	4.36	3.78
Fe I	432.5762	1.610	0.006	2.19	1.31	3.73	1.39	4.19	3.81
Fe II	318.6738	1.700	-1.710	1.69	1.30	4.13	0.90	4.28	4.37
Fe II	319.2909	1.670	-1.950	1.37	1.31	4.20	0.29	4.27	3.87
Fe II	319.3799	1.720	-1.720	1.30	1.31	4.01	0.70	4.27	4.21
Fe II	319.6070	1.670	-1.660	1.61	1.31	4.03	0.44	4.27	3.80
Fe II	321.0444	1.720	-1.790	2.05	1.31	4.36	0.95	4.26	4.52
Fe II	321.3309	1.700	-1.230	1.62	1.31	3.62	–	–	–
Fe II	322.7742	1.670	-1.130	3.29	1.31	4.05	1.94	4.26	4.81
Fe II	325.5887	0.990	-2.500	1.47	1.31	4.19	0.76	4.22	4.31
Fe II	327.7348	0.990	-2.470	1.33	1.31	4.11	0.72	4.20	4.23
Fe II	423.3172	2.580	-1.900	0.51	1.30	4.26	–	–	–
Fe II	492.3927	2.890	-1.320	0.36	1.32	3.77	–	–	–
Fe II	501.8440	2.890	-1.220	0.42	1.33	3.73	0.27	4.08	4.05
Fe II	516.9033	2.890	-0.870	0.65	1.33	3.58	–	–	–
Co I	340.5114	0.430	0.250	1.17	1.32	1.93	2.44	4.12	2.10
Co I	341.2333	0.510	0.030	1.09	1.32	2.05	0.86	4.12	2.02
Co I	345.3508	0.430	0.380	1.54	1.32	1.99	1.41	4.11	1.95

**Table A.1.** Continued.

Specie	$\lambda$ (nm)	$\chi$ (eV)	$\log gf$	$EW_{A,obs}$ (pm)	$f_{A,1D}$	$A(X)_{A,1D}$ (dex)	$EW_{B,obs}$ (pm)	$f_{B,1D}$	$A(X)_{B,1D}$ (dex)
Co I	349.5681	0.630	-0.270	0.65	1.33	2.11	–	–	–
Co I	350.2278	0.430	0.070	1.40	1.33	2.11	–	–	–
Co I	399.5302	0.920	-0.220	0.24	1.29	2.00	0.19	4.48	1.94
Co I	412.1311	0.920	-0.320	0.18	1.31	1.90	–	–	–
Ni I	339.2983	0.030	-0.540	2.66	1.32	2.90	1.57	4.13	2.92
Ni I	343.3554	0.030	-0.668	1.89	1.32	2.77	1.48	4.10	2.93
Ni I	345.2885	0.110	-0.910	1.14	1.32	2.78	1.13	4.11	2.93
Ni I	345.8456	0.210	-0.223	2.25	1.32	2.62	1.32	4.10	2.51
Ni I	346.1649	0.030	-0.347	2.55	1.32	2.67	1.51	4.10	2.66
Ni I	349.2954	0.110	-0.250	2.39	1.33	2.59	1.76	4.07	2.84
Ni I	351.5049	0.110	-0.211	2.74	1.33	2.67	1.74	4.06	2.77
Ni I	352.4535	0.030	0.008	3.90	1.33	2.77	2.12	4.05	2.80
Ni I	361.0461	0.110	-1.149	0.95	1.33	2.92	1.07	4.01	3.05
Ni I	361.9386	0.420	0.035	2.02	1.33	2.46	1.72	4.00	2.75
Ni I	380.7138	0.420	-1.180	1.11	1.30	3.17	0.30	4.38	2.58
Ni I	385.8292	0.420	-0.970	0.73	1.28	2.74	0.68	4.54	2.85

**Table A.2.** Hyperfine structure of Sc and Co

Specie	$\lambda$ (nm)	$\chi$ (eV)	$\log gf$	Specie	$\lambda$ (nm)	$\chi$ (eV)	$\log gf$	Specie	$\lambda$ (nm)	$\chi$ (eV)	$\log gf$
Sc II	361.3815	0.022	-0.126	Co I	341.2328	0.514	-0.171	Co I	350.2241	0.432	-0.221
Sc II	361.3814	0.022	-0.141	Co I	341.2325	0.514	-0.151	Co I	350.2263	0.432	-0.110
Sc II	361.3819	0.022	-0.174	Co I	341.2333	0.514	-0.241	Co I	350.2255	0.432	-0.132
Sc II	361.3817	0.022	-0.108	Co I	341.2330	0.514	-0.151	Co I	350.2245	0.432	-0.231
Sc II	361.3815	0.022	-0.107	Co I	341.2325	0.514	-0.131	Co I	350.2272	0.432	-0.095
Sc II	361.3823	0.022	-0.163	Co I	341.2338	0.514	-0.225	Co I	350.2262	0.432	-0.133
Sc II	361.3821	0.022	-0.096	Co I	341.2333	0.514	-0.141	Co I	350.2251	0.432	-0.251
Sc II	361.3817	0.022	-0.083	Co I	341.2326	0.514	-0.114	Co I	350.2283	0.432	-0.082
Sc II	361.3828	0.022	-0.165	Co I	341.2343	0.514	-0.225	Co I	350.2271	0.432	-0.140
Sc II	361.3825	0.022	-0.090	Co I	341.2336	0.514	-0.136	Co I	350.2257	0.432	-0.291
Sc II	361.3821	0.022	-0.065	Co I	341.2328	0.514	-0.099	Co I	350.2295	0.432	-0.071
Sc II	361.3835	0.022	-0.176	Co I	341.2349	0.514	-0.235	Co I	350.2281	0.432	-0.161
Sc II	361.3831	0.022	-0.089	Co I	341.2341	0.514	-0.137	Co I	350.2308	0.432	-0.060
Sc II	361.3826	0.022	-0.049	Co I	341.2330	0.514	-0.086				
Sc II	361.3843	0.022	-0.198	Co I	341.2356	0.514	-0.256	Co I	384.5473	0.923	-0.180
Sc II	361.3838	0.022	-0.096	Co I	341.2346	0.514	-0.144	Co I	384.5475	0.923	-0.173
Sc II	361.3832	0.022	-0.036	Co I	341.2334	0.514	-0.075	Co I	384.5470	0.923	-0.153
Sc II	361.3853	0.022	-0.238	Co I	341.2364	0.514	-0.295	Co I	384.5479	0.923	-0.243
Sc II	361.3847	0.022	-0.117	Co I	341.2352	0.514	-0.165	Co I	384.5474	0.923	-0.153
Sc II	361.3840	0.022	-0.024	Co I	341.2338	0.514	-0.064	Co I	384.5468	0.923	-0.133
								Co I	384.5480	0.923	-0.227
Sc II	424.6832	0.315	-0.096	Co I	344.9178	0.581	-0.174	Co I	384.5474	0.923	-0.143
Sc II	424.6836	0.315	-0.080	Co I	344.9172	0.581	-0.149	Co I	384.5465	0.923	-0.116
Sc II	424.6836	0.315	-0.039	Co I	344.9183	0.581	-0.149	Co I	384.5481	0.923	-0.227
Sc II	424.6839	0.315	-0.081	Co I	344.9176	0.581	-0.339	Co I	384.5473	0.923	-0.138
Sc II	424.6839	0.315	-0.078	Co I	344.9167	0.581	-0.129	Co I	384.5462	0.923	-0.101
Sc II	424.6841	0.315	-0.098	Co I	344.9183	0.581	-0.129	Co I	384.5482	0.923	-0.237
Sc II	424.6842	0.315	-0.148	Co I	344.9173	0.581	-0.215	Co I	384.5471	0.923	-0.139
Sc II	424.6843	0.315	-0.291	Co I	344.9161	0.581	-0.122	Co I	384.5458	0.923	-0.088
Sc II	424.6843	0.315	-0.096	Co I	344.9182	0.581	-0.122	Co I	384.5483	0.923	-0.257
Sc II	424.6844	0.315	-0.116	Co I	344.9170	0.581	-0.143	Co I	384.5470	0.923	-0.146
Sc II	424.6845	0.315	-0.080	Co I	344.9154	0.581	-0.125	Co I	384.5455	0.923	-0.077
Sc II	424.6846	0.315	-0.098	Co I	344.9181	0.581	-0.125	Co I	384.5483	0.923	-0.297
Sc II	424.6846	0.315	-0.081	Co I	344.9165	0.581	-0.103	Co I	384.5468	0.923	-0.167
				Co I	344.9146	0.581	-0.144	Co I	384.5450	0.923	-0.066
Co I	340.5074	0.432	-0.139	Co I	344.9178	0.581	-0.144				
Co I	340.5072	0.432	-0.159	Co I	344.9159	0.581	-0.074	Co I	399.5299	0.923	-0.203
Co I	340.5081	0.432	-0.159					Co I	399.5304	0.923	-0.203
Co I	340.5079	0.432	-0.138	Co I	345.3472	0.432	-0.105	Co I	399.5302	0.923	-0.305
Co I	340.5075	0.432	-0.137	Co I	345.3479	0.432	-0.150	Co I	399.5297	0.923	-0.175
Co I	340.5088	0.432	-0.137	Co I	345.3475	0.432	-0.093	Co I	399.5306	0.923	-0.175
Co I	340.5085	0.432	-0.124	Co I	345.3489	0.432	-0.250	Co I	399.5302	0.923	-0.235
Co I	340.5081	0.432	-0.126	Co I	345.3485	0.432	-0.129	Co I	399.5296	0.923	-0.161
Co I	340.5098	0.432	-0.126	Co I	345.3480	0.432	-0.081	Co I	399.5308	0.923	-0.161
Co I	340.5093	0.432	-0.107	Co I	345.3498	0.432	-0.229	Co I	399.5302	0.923	-0.190
Co I	340.5088	0.432	-0.122	Co I	345.3493	0.432	-0.119	Co I	399.5294	0.923	-0.154
Co I	340.5110	0.432	-0.122	Co I	345.3488	0.432	-0.070	Co I	399.5310	0.923	-0.154
Co I	340.5104	0.432	-0.090	Co I	345.3510	0.432	-0.226	Co I	399.5302	0.923	-0.157
Co I	340.5097	0.432	-0.123	Co I	345.3504	0.432	-0.115	Co I	399.5292	0.923	-0.153
Co I	340.5123	0.432	-0.123	Co I	345.3497	0.432	-0.059	Co I	399.5313	0.923	-0.153
Co I	340.5116	0.432	-0.074	Co I	345.3524	0.432	-0.234	Co I	399.5302	0.923	-0.131
Co I	340.5108	0.432	-0.131	Co I	345.3517	0.432	-0.117	Co I	399.5290	0.923	-0.160
Co I	340.5139	0.432	-0.131	Co I	345.3508	0.432	-0.050	Co I	399.5315	0.923	-0.160
Co I	340.5131	0.432	-0.060	Co I	345.3540	0.432	-0.253	Co I	399.5302	0.923	-0.109
Co I	340.5121	0.432	-0.152	Co I	345.3531	0.432	-0.125	Co I	399.5288	0.923	-0.180
Co I	340.5156	0.432	-0.152	Co I	345.3522	0.432	-0.041	Co I	399.5317	0.923	-0.180
Co I	340.5147	0.432	-0.046	Co I	345.3558	0.432	-0.292	Co I	399.5302	0.923	-0.090
				Co I	345.3548	0.432	-0.147				
Co I	340.9155	0.514	-0.204	Co I	345.3537	0.432	-0.032	Co I	412.1330	0.923	-0.213
Co I	340.9159	0.514	-0.204					Co I	412.1332	0.923	-0.206
Co I	340.9157	0.514	-0.306	Co I	349.5710	0.629	-0.147	Co I	412.1326	0.923	-0.186
Co I	340.9154	0.514	-0.176	Co I	349.5703	0.629	-0.147	Co I	412.1337	0.923	-0.276
Co I	340.9162	0.514	-0.176	Co I	349.5693	0.629	-0.177	Co I	412.1331	0.923	-0.186
Co I	340.9159	0.514	-0.236	Co I	349.5707	0.629	-0.165	Co I	412.1323	0.923	-0.166
Co I	340.9155	0.514	-0.162	Co I	349.5697	0.629	-0.131	Co I	412.1338	0.923	-0.260
Co I	340.9167	0.514	-0.162	Co I	349.5684	0.629	-0.134	Co I	412.1329	0.923	-0.176
Co I	340.9163	0.514	-0.191	Co I	349.5702	0.629	-0.190	Co I	412.1318	0.923	-0.149
Co I	340.9157	0.514	-0.155	Co I	349.5689	0.629	-0.130	Co I	412.1338	0.923	-0.260
Co I	340.9173	0.514	-0.155	Co I	349.5673	0.629	-0.105	Co I	412.1327	0.923	-0.171
Co I	340.9167	0.514	-0.158	Co I	349.5695	0.629	-0.233	Co I	412.1313	0.923	-0.134
Co I	340.9160	0.514	-0.154	Co I	349.5679	0.629	-0.146	Co I	412.1338	0.923	-0.270
Co I	340.9180	0.514	-0.154	Co I	349.5659	0.629	-0.084	Co I	412.1324	0.923	-0.172
Co I	340.9173	0.514	-0.132					Co I	412.1308	0.923	-0.121
Co I	340.9164	0.514	-0.161	Co I	350.2243	0.432	-0.174	Co I	412.1338	0.923	-0.290
Co I	340.9188	0.514	-0.161	Co I	350.2242	0.432	-0.167	Co I	412.1321	0.923	-0.179
Co I	340.9179	0.514	-0.110	Co I	350.2238	0.432	-0.237	Co I	412.1301	0.923	-0.110
Co I	340.9169	0.514	-0.181	Co I	350.2248	0.432	-0.147	Co I	412.1336	0.923	-0.330
Co I	340.9197	0.514	-0.181	Co I	350.2245	0.432	-0.147	Co I	412.1316	0.923	-0.200
Co I	340.9187	0.514	-0.091	Co I	350.2239	0.432	-0.221	Co I	412.1294	0.923	-0.099
				Co I	350.2255	0.432	-0.127				
Co I	341.2325	0.514	-0.178	Co I	350.2249	0.432	-0.137				